
























# WISDOM project – XI. Star formation efficiency in the bulge of the AGN-host Galaxy NGC 3169 with SITELLE and ALMA

Anan Lu <sup>1</sup>★, Hope Boyce <sup>1</sup>, Daryl Haggard <sup>1</sup>, Martin Bureau <sup>2,3</sup>, Fu-Heng Liang <sup>2</sup>, Lijie Liu <sup>4</sup>, Woorak Choi <sup>3</sup>, Michele Cappellari <sup>2</sup>, Laurent Chemin <sup>5</sup>, Mélanie Chevance <sup>6</sup>, Timothy A. Davis <sup>7</sup>, Laurent Drissen <sup>8</sup>, Jacob S. Elford <sup>7</sup>, Jindra Gensior <sup>9</sup>, J. M. Diederik Kruijssen <sup>6</sup>, Thomas Martin <sup>8</sup>, Etienne Massé <sup>8</sup>, Carmelle Robert <sup>8</sup>, Ilaria Ruffa <sup>7</sup>, Laurie Rousseau-Nepton <sup>10</sup>, Marc Sarzi <sup>11</sup>, Gabriel Savard <sup>8</sup> and Thomas G. Williams <sup>12</sup>

<sup>1</sup>McGill Space Institute and Department of Physics, McGill University, 3600 rue University, Montreal, QC H3A 2T8, Canada

<sup>2</sup>Sub-department of Astrophysics, Department of Physics, University of Oxford, Denys Wilkinson Building, Keble Road, Oxford OX1 3RH, UK

<sup>3</sup>Yonsei Frontier Lab and Department of Astronomy, Yonsei University, 50 Yonsei-ro, Seodaemun-gu, Seoul 03722, Republic of Korea

<sup>4</sup>DTU-Space, Technical University of Denmark, Elektrovej 327, DK-2800 Kgs. Lyngby, Denmark

<sup>5</sup>Centro de Astronomía - CITEVA, Universidad de Antofagasta, Avenida Angamos 601, Antofagasta 1270300, Chile

<sup>6</sup>Astronomisches Rechen-Institut, Zentrum für Astronomie der Universität Heidelberg, Mönchhofstraße 12-14, D-69120 Heidelberg, Germany

<sup>7</sup>Cardiff Hub for Astrophysics Research & Technology, School of Physics & Astronomy, Cardiff University, Queens Buildings, The Parade, Cardiff CF24 3AA, UK

<sup>8</sup>Département de Physique, de Génie Physique et d'Optique, Université Laval, Québec, QC G1V 0A6, Canada

<sup>9</sup>Institute for Computational Science, University of Zürich, Winterthurerstrasse 190, CH-8057 Zürich, Switzerland

<sup>10</sup>Canada–France–Hawaii Telescope, Kamuela, HI 96743, USA

<sup>11</sup>Armagh Observatory and Planetarium, College Hill, Armagh BT61 9DG, UK

<sup>12</sup>Max Planck Institut für Astronomie, Königstuhl 17, D-69117 Heidelberg, Germany

Accepted 2022 May 28. Received 2022 May 25; in original form 2022 February 22

## ABSTRACT

The star formation efficiency (SFE) has been shown to vary across different environments, particularly within galactic starbursts and deep within the bulges of galaxies. Various quenching mechanisms may be responsible, ranging from galactic dynamics to feedback from active galactic nuclei (AGNs). Here, we use spatially resolved observations of warm ionized gas emission lines ( $H\beta$ ,  $[O\text{ III}] \lambda\lambda 4959, 5007$ ,  $[N\text{ II}] \lambda\lambda 6548, 6583$ ,  $H\alpha$  and  $[S\text{ II}] \lambda\lambda 6716, 6731$ ) from the imaging Fourier transform spectrograph SITELLE at the Canada–France–Hawaii Telescope (CFHT) and cold molecular gas ( $^{12}\text{CO}(2-1)$ ) from the Atacama Large Millimeter/sub-millimeter Array (ALMA) to study the SFE in the bulge of the AGN-host galaxy NGC 3169. After distinguishing star-forming regions from AGN-ionized regions using emission-line ratio diagnostics, we measure spatially resolved molecular gas depletion times ( $\tau_{\text{dep}} \equiv 1/\text{SFE}$ ) with a spatial resolution of  $\approx 100$  pc within a galactocentric radius of 1.8 kpc. We identify a star-forming ring located at radii  $1.25 \pm 0.6$  kpc with an average  $\tau_{\text{dep}}$  of 0.3 Gyr. At radii  $< 0.9$  kpc, however, the molecular gas surface densities and depletion times increase with decreasing radius, the latter reaching approximately 2.3 Gyr at a radius  $\approx 500$  pc. Based on analyses of the gas kinematics and comparisons with simulations, we identify AGN feedback, bulge morphology and dynamics as the possible causes of the radial profile of SFE observed in the central region of NGC 3169.

**Key words:** ISM: clouds – H II regions – galaxies: bulges – galaxies: individual: NGC 3169 – galaxies: ISM – galaxies: nuclei.

## 1 INTRODUCTION

The tight correlation between the star formation rates (SFRs) and stellar masses ( $M_*$ ) of galaxies, referred to as the star formation main sequence (SFMS; e.g. Brinchmann et al. 2004; Noeske et al. 2007; Rodighiero et al. 2011; Speagle et al. 2014), suggests a self-regulated evolution of galaxy mass and size (Bouché et al. 2010; Genzel et al. 2010; Davé, Finlator & Oppenheimer 2012; Feldmann & Mayer 2015). However, many galaxies deviate from the SFMS, particularly

the ‘quenched’ galaxy population, which has much lower specific star formation rates (sSFRs; i.e.  $\text{SFR}/M_*$ ). Our understanding of this star formation truncation remains poor, with galactic dynamics (e.g. Martig et al. 2009, 2013; Gensior, Kruijssen & Keller 2020), mergers (e.g. Moustakas et al. 2013) and/or active galactic nuclei (AGNs) feedback (e.g. Pontzen et al. 2017) all offering possible contributing mechanisms.

Fundamentally, stars should form from the cold and dense (typically molecular) gas in the interstellar medium (ISM). Star formation quenching is therefore either the result of a low molecular gas fraction ( $f_{\text{H}_2}$ ;  $f_{\text{H}_2} \equiv \frac{M_{\text{H}_2}}{M_*}$ ) and/or a low star formation efficiency (SFE);

\* E-mail: [anan.lu@mail.mcgill.ca](mailto:anan.lu@mail.mcgill.ca)

SFE  $\equiv$  SFR/ $M_{\text{H}_2}$ ), as the reduction of either of them would lead to a lower sSFR. In turn, the depletion time ( $\tau_{\text{dep}}$ ;  $\tau_{\text{dep}} \equiv \text{SFE}^{-1} = \frac{M_{\text{H}_2}}{\text{SFR}}$ ), i.e. the time-scale required to exhaust the molecular gas present at the current SFR, is a useful quantity to probe star formation. The power-law relation between  $M_{\text{H}_2}$  and SFR on galactic scales (Kennicutt 1998; Kennicutt & De Los Reyes 2021) shows that  $\tau_{\text{dep}}$  of starburst galaxies is  $10\text{--}10^2$  Myr, while those of spiral galaxies tend to be much longer, reaching over  $10^3$  Myr. On sub-galactic scales, where  $\tau_{\text{dep}}$  is typically calculated as the ratio of the molecular gas mass surface density ( $\Sigma_{\text{H}_2}$ ) to the SFR surface density ( $\Sigma_{\text{SFR}}$ ), Bigiel et al. (2008) revealed a depletion time of  $\approx 2$  Gyr.

Within individual galaxies, evidence also suggests that the SFE is not uniform across the variety of local environments (e.g. disc, spheroid, spiral arms, inter-arm regions; Querejeta et al. 2019). Contrary to the high SFEs of starburst regions, the SFEs are reduced in galaxy bulges (e.g. Davis et al. 2014; Kruijssen et al. 2014). The SFRs of early-type galaxies (ETGs) and bulges are also suppressed by a factor of  $\approx 2.5$  compared to those of spiral galaxy discs with similar molecular gas mass surface densities (e.g. Saintonge et al. 2011). It is possible that this star formation suppression is analogous to that observed in the central regions of spirals and growing spheroids at higher redshifts (Lang et al. 2014), and it may therefore be a symptom of a more general process. Indeed, the central molecular zone (CMZ), i.e. the inner  $\approx 500$  pc in radius of our own Milky Way, also has an SFR one order of magnitude smaller than the Galactic average, despite very high molecular gas mass surface densities (e.g. Longmore et al. 2013). A multitude of physical processes have been implicated, but the high turbulent pressure within the CMZ is likely the most important (Kruijssen et al. 2014).

It is therefore crucial to compare different environments to validate commonly postulated quenching mechanisms, such as ‘morphological quenching’, where a nearly spherical potential holds gas stable against star formation (e.g. Martig et al. 2009, 2013; Gensior et al. 2020), dynamical processes such as shear and tides, that stabilise the gas clouds against gravitational collapse (e.g. Davis et al. 2014; Kruijssen et al. 2019a; Liu et al. 2021), and AGN feedback, whereby radiation and jets from AGN physically remove and/or heat up the gas (e.g. Pontzen et al. 2017).

To distinguish these different mechanisms in the inner regions of galaxies, we have initiated a project to measure the SFEs of galaxy bulges in a spatially resolved manner, combining high-spatial resolution  $^{12}\text{CO}(2-1)$  measurements (by a cold gas indicator) from the Atacama Large Millimeter/sub-millimeter Array (ALMA) with ionized hydrogen emission-line measurements (by an SFR indicator) from the imaging Fourier transform spectrograph SITELLE at the Canada–France–Hawaii Telescope (CFHT). Here, we present a pilot study based on a single galaxy, the nearby early-type spiral galaxy NGC 3169 with a mean SFR of  $\approx 2 M_{\odot} \text{ yr}^{-1}$ . This galaxy has a dense bulge (with an effective radius  $\approx 1.4$  kpc and a Sérsic index of  $\approx 4.17$ ; from Dong & De Robertis 2006) and a low-luminosity AGN (LLAGN; e.g. Ghosh et al. 2008; Mathur et al. 2008), making it ideal for a deep investigation of various quenching mechanisms. The target and observations are described in Section 2, followed by surface-density and line-ratio maps in Section 3. In Section 4, we calculate depletion times and examine the radial trend of SFE and its correlation with galaxy dynamics (i.e. the virial parameters of the H II regions and galaxy velocity field). In Section 5, we discuss the mechanisms contributing to the radial profile of SFE in the central region, including AGN feedback, bulge morphology and dynamics. We conclude and discuss future work in Section 6.

## 2 OBSERVATIONS AND DATA REDUCTION

### 2.1 NGC 3169

NGC 3169 is an S(a) spiral galaxy at a distance  $D = 18.7$  Mpc, according to the NASA Extragalactic Database redshift-independent distance catalogue (Steer et al. 2017). It has an inclination  $i = 54^\circ$ , a position angle  $PA = 45^\circ$  and a systemic heliocentric velocity  $V_{\text{sys}} = 1232 \text{ km s}^{-1}$  (from the H I 21-cm observations of Lee-Waddell et al. 2012, consistent with the best-fitting systemic velocity derived from our own CO data discussed in Section 4.5). NGC 3169 is representative of early-type spiral galaxies, while interacting with its close companion galaxy NGC 3166 (Sil’chenko & Afanasiev 2006). It hosts a complex central region, consisting of a dense and clear bulge, a small-scale bar, an AGN and a young nucleus, making it possible to probe multiple components that can affect local SFE. Fig. 1 shows a deep image produced from our SITELLE observations of NGC 3169, overlaid with contours of H $\alpha$  flux (measured with SITELLE) and  $^{12}\text{CO}(2-1)$  flux (measured with ALMA).

The H I gas mass of NGC 3169 is  $(4.2 \pm 0.5) \times 10^9 M_{\odot}$  (Lee-Waddell et al. 2012). The ultraviolet and infrared images from the *Wide-field Infrared Survey Explorer* (WISE) and *Galaxy Evolution Explorer* (GALEX) missions (Leroy et al. 2019) indicate a stellar mass of  $\log(M_{\star}/M_{\odot}) \approx 10.84$  and an SFR  $\log(\text{SFR}/M_{\odot} \text{ yr}^{-1}) \approx 0.29$  within a central aperture of diameter  $\approx 19'$ . Key parameters of NGC 3169 are summarized in Table 1.

Probing the centre of NGC 3169, Sil’chenko & Afanasiev (2006) obtained spatially resolved measurements in the wavelength range 4200–5600 Å from the Multi Pupil Fiber Spectrograph (MPFS) at the prime focus of the 6-m Special Astrophysical Observatory (SAO) telescope. They reported a young stellar population with an estimated age of 1–2 Gyr in the central region, including a star-like nucleus and a ring of young stars 6 arcsec ( $\approx 600$  pc) from the centre. Within the nuclear region (radius  $\lesssim 200$  pc), Dong & De Robertis (2006) reported an H $\alpha$  luminosity  $\approx 10^{39} \text{ erg s}^{-1}$ , based on a spectroscopic survey carried out with the 5-m telescope at Mount Palomar by Ho, Filippenko & Sargent (1997). Integrated emission-line ratios in this region were reported as H $\alpha$ /H $\beta$  = 5.03, [O III] $\lambda$ 5007/H $\beta$  = 2.88, and [N II] $\lambda$ 6583/H $\alpha$  = 2.07, indicating the presence of an AGN.

Furthermore, Dong & De Robertis (2006) used the GALFIT software (Peng et al. 2002) on Two Micron All Sky Survey (2MASS)  $K_s$ -band images to decompose the galaxy into a spheroidal bulge and an exponential disc. They reported bulge and disc  $K_s$ -band integrated apparent magnitudes  $m_{\text{bul}} = 7.52$  and  $m_{\text{disc}} = 8.42$ . The effective radius of the bulge component is  $15''.7$  or 1.4 kpc at our assumed distance. Based on this bulge-disc decomposition, we estimate the enclosed bulge-to-disc luminosity ratio (B/D) as a function of galactocentric radius; B/D approaches unity at a radius of  $\approx 660$  pc. This suggests that the bulge is dominating over the disc within  $\approx 660$  pc radius, while the impact from the bulge can reach over 1.4 kpc.

The presence of a low-luminosity AGN (LLAGN) at the heart of NGC 3169 has been confirmed at multiple wavelengths. Based on *Chandra* X-ray data, Ghosh et al. (2008) reported a hard X-ray detection and fitted the spectrum with an absorbed power law, deriving a power-law index  $\Gamma \approx 2$  and a hydrogen column density  $N_{\text{H}} \approx 10^{23} \text{ cm}^{-2}$ . They inferred an unabsorbed broad-band X-ray flux  $f_{0.3-8 \text{ keV}} = 1 \times 10^{-11} \text{ erg cm}^{-2} \text{ s}^{-1}$ , equivalent to a luminosity  $L_{0.3-8 \text{ keV}} = 1.1 \times 10^{41} \text{ erg s}^{-1}$  at our assumed distance. A milliarcsecond-scale radio source was also detected, with a 5-GHz flux  $f_{5 \text{ GHz}} = 6.6 \times 10^{-26} \text{ erg cm}^{-2} \text{ s}^{-1} \text{ Hz}^{-1}$ . The measured

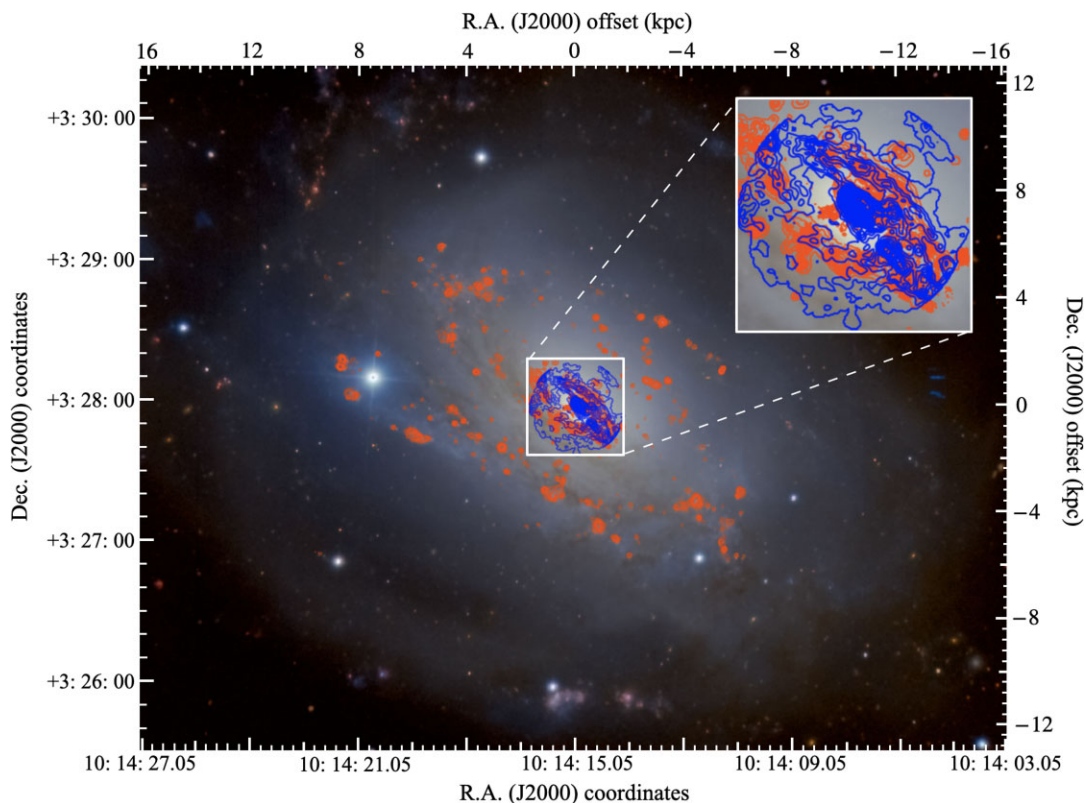


**Figure 1.** Deep image of NGC 3169 extracted from the CFHT SITELLE observations discussed in Section 2.2, with the  $H\alpha$  integrated intensity overlaid as orange contours and the CO integrated intensity (extracted from the ALMA observations discussed in Section 2.3) overlaid as blue contours. The white box indicates the central  $\approx 3.6 \times 3.6$  kpc<sup>2</sup> region, encompassing the galaxy bulge, which is the main focus of this paper. The inset shows a zoom-in view of the central region.

brightness temperature exceeds  $10^{7.7}$  K, ruling out a starburst and/or supernova remnant origin, thus confirming the presence of an LLAGN (Nagar, Falcke & Wilson 2005). Following the bulge-disc decomposition summarized above, Dong & De Robertis (2006) estimated a central supermassive black hole mass  $\log(M_{\bullet}/M_{\odot}) = 8.2$  using their derived bulge mass – black hole mass correlation based on 117 galaxies. Separately, Héraudeau et al. (1999) reported a central stellar velocity dispersion  $\sigma_{\ast} = 163$  km s<sup>-1</sup>, corresponding to  $\log(M_{\bullet}/M_{\odot}) = 7.8$  using the stellar velocity dispersion – black hole mass correlation of Kormendy & Ho (2013). Taking the average of these two black hole mass estimates, the Eddington luminosity is estimated to be  $L_{\text{Edd}} \approx 10^{46}$  erg s<sup>-1</sup> (Ghosh et al. 2008). With this well-characterized LLAGN at the centre, the potential influence of AGN feedback on star formation in the bulge of NGC 3169 can be uniquely probed.

## 2.2 Ionized gas data

NGC 3169 was observed with SITELLE (Drissen et al. 2019) at CFHT during the 2020B semester (programme number 20Bc25). The observations were centred at RA (J2000) =  $10^{\text{h}}14^{\text{m}}15^{\text{s}}.05$  and Dec. (J2000) =  $3^{\circ}27'57''.90$ . SITELLE is an optical imaging Fourier transform spectrograph (IFTS) equipped with two E2V detectors each with  $2048 \times 2064$  pixels. The field of view (FOV) is  $11 \times 11$  arcmin<sup>2</sup>, resulting in a mean spaxel size on the sky of  $0''.31 \times 0''.31$  (or  $28 \times 28$  pc<sup>2</sup>). Two datacubes were obtained: one centred on the emission lines of [N II] $\lambda$ 6548,  $H\alpha$ , [N II] $\lambda$ 6583, [S II] $\lambda$ 6716, and [S II] $\lambda$ 6731 with the SN3 filter (6480–6860 Å) at a mean spectral resolution of  $R \approx 2000$ ; the other centred on the emission lines of

$H\beta$ , [O III] $\lambda$ 4959 and [O III] $\lambda$ 5007 with the SN2 filter (4840–5120 Å) at a mean spectral resolution  $R \approx 900$ .

The data reduction was performed with the ORBS software developed for SITELLE (Martin, Drissen & Joncas 2015; Martin, Drissen & Prunet 2021). The seeing was measured to be  $1''.1$  (or 99 pc) from the full width at half-maxima (FWHM) of Gaussian fits to foreground stars from the Gaia catalogue (Lindegren et al. 2018). The data were further calibrated in wavelength based on velocity measurements of the OH sky line. As a final pre-processing step, sky background subtraction was performed using a median sky spectrum extracted from a  $200 \times 200$  spaxels region located far away from the galaxy disc. The emission lines in each spaxel were then fitted using the extraction software ORCS (Martin et al. 2015). For each emission line, maps of flux, mean velocity, and velocity dispersion were generated from ORCS output parameters including integrated flux within each spaxel, maximum intensity, velocity, FWHM, continuum level and signal-to-noise ratio ( $S/N$ ) of the spectrum as well as their uncertainties. Modelling the sinc-Gauss profile of the emission lines allows to measure velocity dispersions much smaller than the nominal spectral resolution, provided that the  $S/N$  is sufficient (Martin, Prunet & Drissen 2016). A detection threshold was then applied based on the  $3\sigma$  noise level of the  $H\alpha$ + [N II] flux. For illustration purposes, the full set of  $H\alpha$  maps (before extinction correction) and the [N II] $\lambda$ 6583 velocity dispersion map used for this work are presented in Fig. 2. The extinction correction and conversion of the  $H\alpha$  flux to  $\Sigma_{\text{SFR}}$  are discussed in Section 3.1. We use the ratios of these emission lines to correctly identify the H II regions and examine the extent of the AGN impact in Sections 3.3 and 5.



**Table 1.** Key parameters of NGC 3169.

| Reference | Quantity  | Value   |
|-----------|---|---|
| (1)       | Type  | SA(s)a pec  |
| (2)       | RA  | 10 <sup>h</sup> 14 <sup>m</sup> 15 <sup>s</sup> .05 |
| (3)       | DEC   | 3°27′57″.90   |
| (4)       | Distance (Mpc)  | 18.7  |
| (5)       | log( $M_{\text{H}_2} / M_{\odot}$ )   | 9.32  |
| (6)       | log( $\Sigma_{\text{H}_2, 2 \text{ kpc}} / M_{\odot} \text{ pc}^{-2}$ )                   | 2.31  |
| (7)       | log( $M_{\star} / M_{\odot}$ )  | 10.84   |
| (8)       | $\sigma_{\star}$ (km s <sup>-1</sup> )  | 163   |
| (9)       | log( $\mu_{\star} / M_{\odot} \text{ kpc}^{-2}$ )   | 8.26  |
| (10)      | log (sSFR / yr <sup>-1</sup> )  | -10.55  |
| (11)      | $R_{e, \text{KS}}$ (″)  | 85.7  |
| (12)      | log (SFR / $M_{\odot} \text{ yr}^{-1}$ )  | 0.29  |
| (13)      | log ( $\Sigma_{\text{SFR}, 2 \text{ kpc}} / M_{\odot} \text{ yr}^{-1} \text{ kpc}^{-2}$ ) | -0.67   |
| (14)      | $L_{\text{Edd}}$ (erg s <sup>-1</sup> )   | ≈10 <sup>46</sup>                                   |

*Notes.* Column (1) – morphology of the galaxy taken from de Vaucouleurs et al. (1991). Columns (2) and (3) are the RA–Dec. coordinate of the galaxy center used for SITESLE observations and referenced for all the maps in this work. Column (4) – assumed distance taken from the NASA extragalactic database redshift independent distance catalogue (Steer et al. 2017). Column (5) – molecular gas mass measured within our ALMA field of view as described in Section 3.2 Column (6) – mean molecular gas surface density measured within the inner 2 kpc of the galaxy, as described in Section 3.2. Column (7) – stellar mass of the galaxy taken from Leroy et al. (2019). Column (8) – stellar velocity dispersion taken from Héraudeau et al. (1999). Column (9) – stellar mass surface density ( $\mu_{\star} = M_{\star} / (2\pi R_{\text{e}}^2)$ ) estimated within the effective radius ( $R_{\text{e, KS}}$ ) of the galaxy. Column (10) – specific star formation rate (sSFR =  $M_{\star} / \text{SFR}$ ) calculated based on columns (7) and (12). Column (11) –  $K_s$ -band effective radius estimated from the 2  $\mu\text{m}$  all-sky survey (2MASS; Jarrett et al. 2003). Column (12) – total SFR taken from Leroy et al. (2019). Column (13) – mean SFR surface density measured within the inner 2 kpc of the galaxy, as described in Section 3.1. Column (14) – estimated Eddington luminosity of the supermassive black hole, taken from Ghosh et al. (2008).

### 2.3 Molecular gas data

The NGC 3169 molecular gas data used were obtained in the <sup>12</sup>CO(2-1) line (230 GHz) using ALMA in January 2015 (configuration: C36-4; programme: 2015.1.00598.S; PI: Bureau) and January 2016 (configuration: 7M; programme: 2016.2.00053.S; PI: Liu), as part of the mm-Wave Interferometric Survey of Dark Object Masses (WISDOM) project (Onishi et al. 2017). The first observation (2015.1.00598.S) obtained 605 s on the source using 38 12-m antennae, resulting in a primary beam (FWHM) of 27′.4 and a maximum recoverable scale of 5′.8. The intrinsic channel width was 1.27 km s<sup>-1</sup> (977 kHz). The line was covered by a correlator window of 1.875 GHz, equivalent to 2450 km s<sup>-1</sup>. The second observation obtained 1120 s on source using eight 7-m antennae, that extended the primary beam (FWHM) to 45′.7 and the maximum recoverable scale to 36′.4. The line was covered by a correlator window of 2 GHz.

The raw ALMA data were reduced using the Common Astronomy Software Applications (CASA) pipeline (version 5.3), which automatically processes the data by performing basic flagging and calibration (McMullin et al. 2007). The two ALMA observations were then combined using the CASA task `concat`. Continuum emission was detected, measured over the full line-free bandwidth, and then subtracted from the data in the  $uv$  plane using the CASA task `uvcontsub`. The data were then imaged using the CASA task `clean` (version 5.6.1), adopting a channel width of 2 km s<sup>-1</sup>, a Briggs’ weighting robust parameter of 2.0 and a  $uv$ -taper of 0′.7, thus achieving a synthesised beam size (FWHM) of 0′.99 × 0′.84 (89 pc × 76 pc) at a position angle of -58°, roughly matching the

seeing of the H $\alpha$  observations. Finally, we convolved this datacube spatially by a narrow and slightly elongated two-dimensional (2D) Gaussian, to achieve a perfectly circular synthesized beam of FWHM 1′.1, thus perfectly matching the seeing of the H $\alpha$  observations. This produced our final fully calibrated and continuum-subtracted <sup>12</sup>CO(2-1) datacube of NGC 3169, with a mean RMS noise level of 3.06 mJy beam<sup>-1</sup> per 2 km s<sup>-1</sup> channel, although we also performed primary beam correction for the imaging of moment maps. Sky coordinates and spaxel size of the datacube were also matched to those of the SITESLE datacubes. Finally, another datacube was produced following the same procedure but with a channel width of 15 km s<sup>-1</sup>, to enhance the S/N for the purpose of the gas kinematics analyses carried out in Section 4.5.

The integrated <sup>12</sup>CO(2-1) spectrum and moment-0 (integrated flux), moment-1 (mean velocity) and moment-2 (velocity dispersion) maps are shown in Fig. 3. The 230-GHz continuum map is also shown in Fig. 3 and reveals a bright region at the galaxy centre, slightly extended along the disc major axis and with an integrated flux of 8.5 mJy, that could be explained by dust or a jet from the LLAGN. The one-sided structure of this continuum source favours the explanation of a jet, although some VLA radio maps (in e.g. Nagar et al. 2005) show extended structure in the perpendicular direction. Higher resolution observations are needed to resolve the existence and morphology of the jet. Nevertheless, the strong and broadened N II emission lines at this location indicate the existence of AGN-driven outflows or a supernova very close to the LLAGN. A recent spectral energy distribution (SED) analysis of the source also reveals a negative spectral index consistent with synchrotron emission (Elford et al., in preparation).

The physical scale of the synthesized beam (99 pc) allows to estimate the molecular gas mass surface density and thus (combined with H $\alpha$ ) the SFE at the typical spatial scale of giant molecular clouds (GMCs; ≈50 pc; Rosolowsky et al. 2003, 2007) and H II regions of similar sizes. Stand-alone GMC analyses should however be performed at the highest angular resolution possible for the CO data, here 0′.58 × 0′.58 (52 × 52 pc<sup>2</sup>), when adopting a more standard Briggs’ robust parameter of 0.5 and no taper.

## 3 SURFACE DENSITIES AND LINE RATIO

### 3.1 SFR surface densities

We correct the observed H $\alpha$  fluxes ( $F_{\text{H}\alpha, \text{obs}}$ ) for extinction using the observed H $\beta$  fluxes ( $F_{\text{H}\beta, \text{obs}}$ ) and the assumed Balmer decrement described below. Due to differences in the spectral resolutions and observing conditions of the two SITESLE datacubes, the H $\beta$  spaxels that satisfy a 3 $\sigma$  detection threshold only constitute 52 per cent of the H $\alpha$  spaxels satisfying that same condition. For each spaxel with both the H $\alpha$  and H $\beta$  lines satisfying the 3 $\sigma$  detection threshold, the ‘colour excess’ of H $\alpha$  over H $\beta$  is defined as

$$E(\text{H}\beta - \text{H}\alpha) \equiv 2.5 \log \left( \frac{(F_{\text{H}\alpha, \text{obs}}/F_{\text{H}\beta, \text{obs}})}{(H\alpha/H\beta)_{\text{init}}} \right), \quad (1)$$

where we assume  $(H\alpha/H\beta)_{\text{init}} = 2.86$ , as expected for the case B recombination at a temperature of 10<sup>4</sup> K (Osterbrock & Ferland 2006).

The H $\alpha$  extinction is then calculated as

$$A_{\text{H}\alpha} = \left( \frac{E(\text{H}\beta - \text{H}\alpha)}{k(\lambda_{\text{H}\beta}) - k(\lambda_{\text{H}\alpha})} \right) k(\lambda_{\text{H}\alpha}) \quad (2)$$

following Nelson et al. (2016), where  $k(\lambda)$  is the reddening curve of Fitzpatrick (1986) and  $k(\lambda_{\text{H}\alpha})$  and  $k(\lambda_{\text{H}\beta})$  are evaluated at the

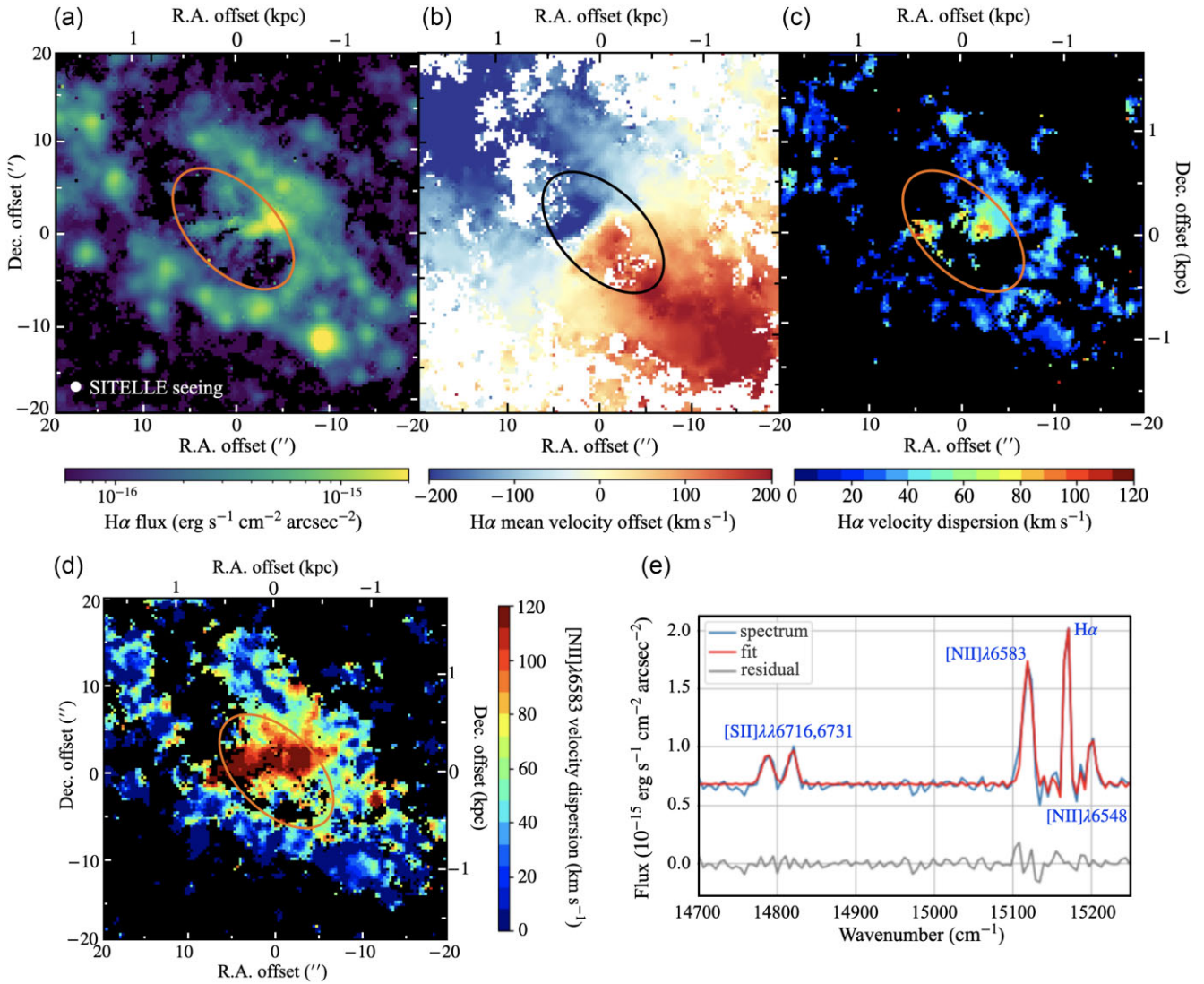


**Figure 2.** Top row: H $\alpha$  maps of the central region of NGC 3169 ( $\approx 3.6 \times 3.6$  kpc $^2$ ), encompassing the galaxy bulge, extracted from our SITELLE SN3 datacube using the sinc-Gauss line-fitting function in ORCS as described in Section 2.2. Panel (a): integrated intensity map. Panel (b): mean velocity map, with respect to the heliocentric velocity of the galaxy (1232 km s $^{-1}$ , see Section 2.1). Panel (c): velocity dispersion map. Panel (d): [N II]  $\lambda$  6583 velocity dispersion map of the same region. The orange and black ellipses in panels (a)–(d) separate the inner disc and outer star-forming ring discussed in Sections 4–5. Panel (e): sample spectrum (blue line) containing the emission lines [N II]  $\lambda$  6548, H $\alpha$ , [N II]  $\lambda$  6583, [S II]  $\lambda$  6716, and [S II]  $\lambda$  6731. The ORCS-fitted spectrum is shown as a red line, while the residuals are shown as a grey line and shifted lower for illustration purposes.

wavelengths of H $\alpha$  and H $\beta$ , respectively. For each spaxel with a  $3\sigma$  H $\alpha$  detection but no  $3\sigma$  H $\beta$  detection, we adopt the H $\alpha$  extinction of the nearest reliable spaxel. The extinction-corrected H $\alpha$  flux of each spaxel is then obtained as

$$F_{\text{H}\alpha} = F_{\text{H}\alpha, \text{obs}} e^{A_{\text{H}\alpha}/1.086}. \quad (3)$$

This extinction-corrected H $\alpha$  flux is converted into an SFR using the relation of Kennicutt & Evans (2012):

$$\log(\text{SFR} / M_{\odot} \text{ yr}^{-1}) = \log(L_{\text{H}\alpha} / \text{ergs s}^{-1}) - 41.27, \quad (4)$$

where  $L_{\text{H}\alpha} = F_{\text{H}\alpha}(4\pi D^2)$  is the extinction-corrected H $\alpha$  luminosity. We note that when probing spatial scales smaller than 500 pc, this conversion relation can break down, as seen in examples of Kennicutt & Evans (2012). Local SFR depend on environments and age of the stellar population that we can only estimate here. Nevertheless, this conversion holds true for the radial profile of SFE (see Section 4.3),

which is calculated within apertures large enough for confident H $\alpha$ –SFR conversions.

The  $\Sigma_{\text{SFR}}$  is then calculated as the SFR within each spaxel divided by the spaxel area. The mean  $\Sigma_{\text{SFR}}$  in the central region of NGC 3169,  $\log(\Sigma_{\text{SFR}, 2 \text{ kpc}} / M_{\odot} \text{ yr}^{-1} \text{ kpc}^{-2}) = -0.67$ , is calculated from the total SFR within a radius of  $\approx 1.8$  kpc, as listed in Table 1.

### 3.2 Molecular gas mass surface densities

A map of the molecular gas mass surface density ( $\Sigma_{\text{H}_2}$ ) can be obtained from the  $^{12}\text{CO}(2-1)$  observations described in Section 2.3. First, the CO flux ( $F_{\text{CO}(2-1)}$ ) within each spaxel is obtained from the moment-0 map fluxes (in Jy beam $^{-1}$  km s $^{-1}$ ) by dividing by the synthesised beam area in spaxels.  $F_{\text{CO}(2-1)}$  is then converted into luminosity according to

$$\frac{L_{\text{CO}(2-1)}}{\text{K km s}^{-1} \text{ pc}^2} = \left( \frac{3.25 \times 10^7}{(1+z)^3} \right) \left( \frac{F_{\text{CO}(2-1)}}{\text{Jy km s}^{-1}} \right) \left( \frac{v_{\text{obs}}}{\text{GHz}} \right)^{-2} \left( \frac{D}{\text{Mpc}} \right)^2 \quad (5)$$

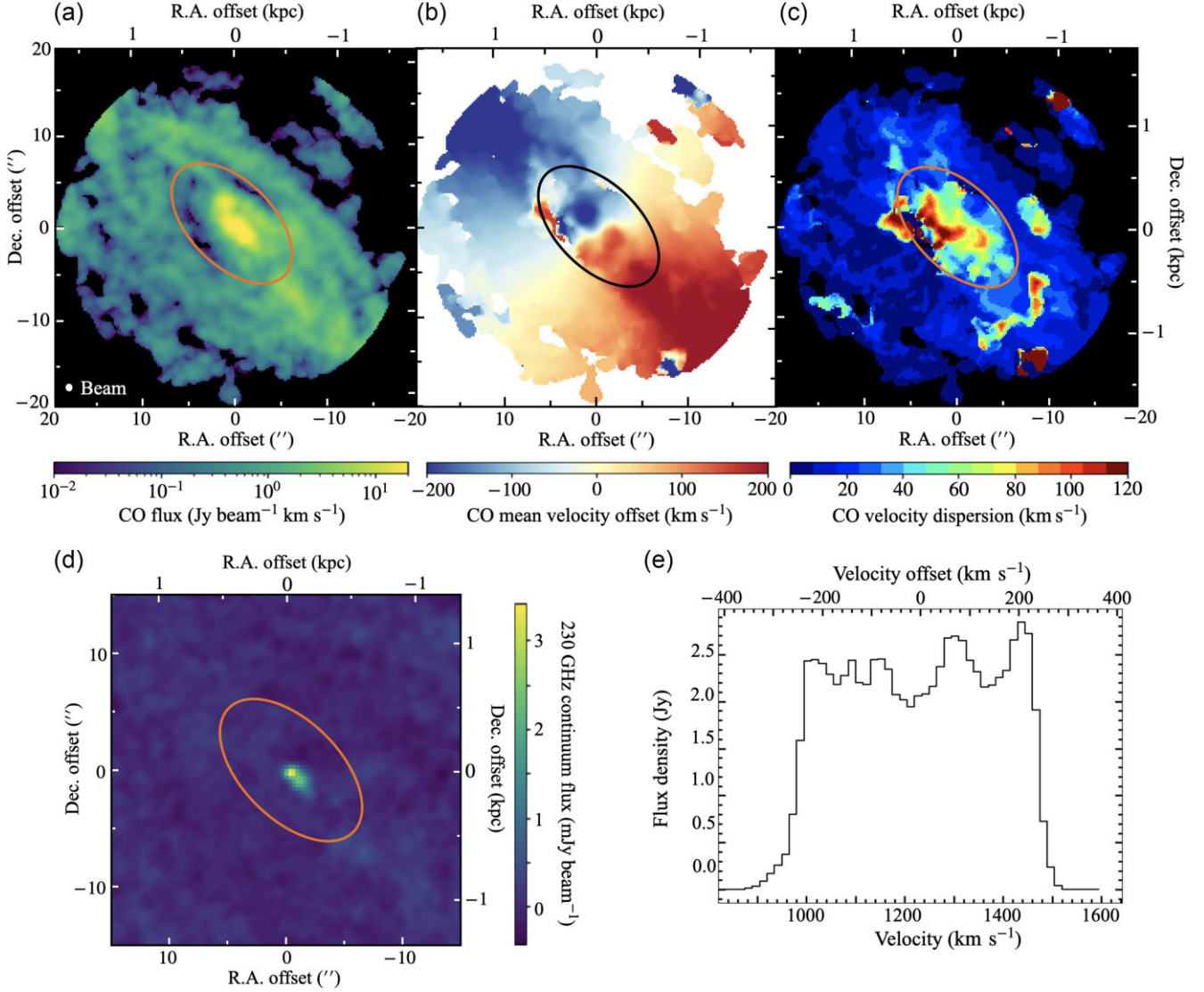


**Figure 3.** Top row:  $^{12}\text{CO}(2-1)$  maps of the central region of NGC 3169 ( $\approx 3.6 \times 3.6$  kpc $^2$ ), encompassing the galaxy bulge, extracted from our ALMA observations as described in Section 2.3. Panel (a): Moment-0 (integrated intensity) map. Panel (b): Moment-1 (mean velocity) map, with respect to the heliocentric velocity of the galaxy of (1232 km s $^{-1}$ ; see Section 2.1). Panel (c): Moment-2 (velocity dispersion) map. Panel (d): 230-GHz continuum emission map. The orange and black ellipses in Panels (a)–(d) separate the inner disc and outer star-forming ring discussed in Sections 4–5. Panel (e):  $^{12}\text{CO}(2-1)$  spectrum integrated over the whole field of view of the 15 km s $^{-1}$  per channel datacube.

(e.g. Decarli et al. 2016), where  $z$  is the galaxy redshift and  $\nu_{\text{obs}}$  is the observed frequency [i.e. the redshifted frequency of the CO(2-1) line]. The luminosity-based molecular gas mass within each spaxel is then calculated using

$$\frac{M_{\text{H}_2}}{M_{\odot}} = 4.4 \left( \frac{L_{\text{CO}}}{\text{K km s}^{-1} \text{ pc}^2} \right) \left( \frac{X_{\text{CO}}}{2 \times 10^{20} \text{ cm}^{-2} (\text{K km s}^{-1})^{-1}} \right), \quad (6)$$

where  $L_{\text{CO}}$  is the CO(1-0) luminosity and  $X_{\text{CO}}$  is the CO-to- $\text{H}_2$  conversion factor. We adopt a CO(2-1)/CO(1-0) ratio of 0.8 (in brightness temperature units), typical of spiral galaxies (e.g. Lamperti et al. 2020), and  $X_{\text{CO}} = 2.3 \times 10^{20} \text{ cm}^{-2} (\text{K km s}^{-1})^{-1}$ . The adopted  $X_{\text{CO}}$  is commonly used in extragalactic studies (e.g. Hughes et al. 2013; Utomo et al. 2015; Sun et al. 2018), although it can depend on the environment of molecular clouds, such as metallicity and radiation field (Bolatto, Wolfire & Leroy 2013). The mass contribution from helium is considered and included in the coefficient (Strong et al. 1988; Bolatto et al. 2013). The complete conversion

thus becomes

$$\frac{M_{\text{H}_2}}{M_{\odot}} = 6.325 \left( \frac{L_{\text{CO}(2-1)}}{\text{K km s}^{-1} \text{ pc}^2} \right). \quad (7)$$

The molecular gas mass surface density is then calculated as  $M_{\text{H}_2}$  divided by the spaxel area. The mean  $\Sigma_{\text{H}_2}$  in the central region of NGC 3169,  $\log(\Sigma_{\text{H}_2, 2 \text{ kpc}} / M_{\odot} \text{ pc}^{-2}) = 2.31$ , is calculated from the total molecular gas mass within a radius of  $\approx 1.8$  kpc, as listed in Table 1.

### 3.3 Emission-line ratios

Considering the existence of the LLAGN at the centre of NGC 3169, it is unclear what fraction of the  $\text{H}\alpha$  emission originates from star formation, especially within a 1 kpc radius of the galaxy centre. To accurately determine the SFEs in this region, we must distinguish the different ionization mechanisms and confidently identify the



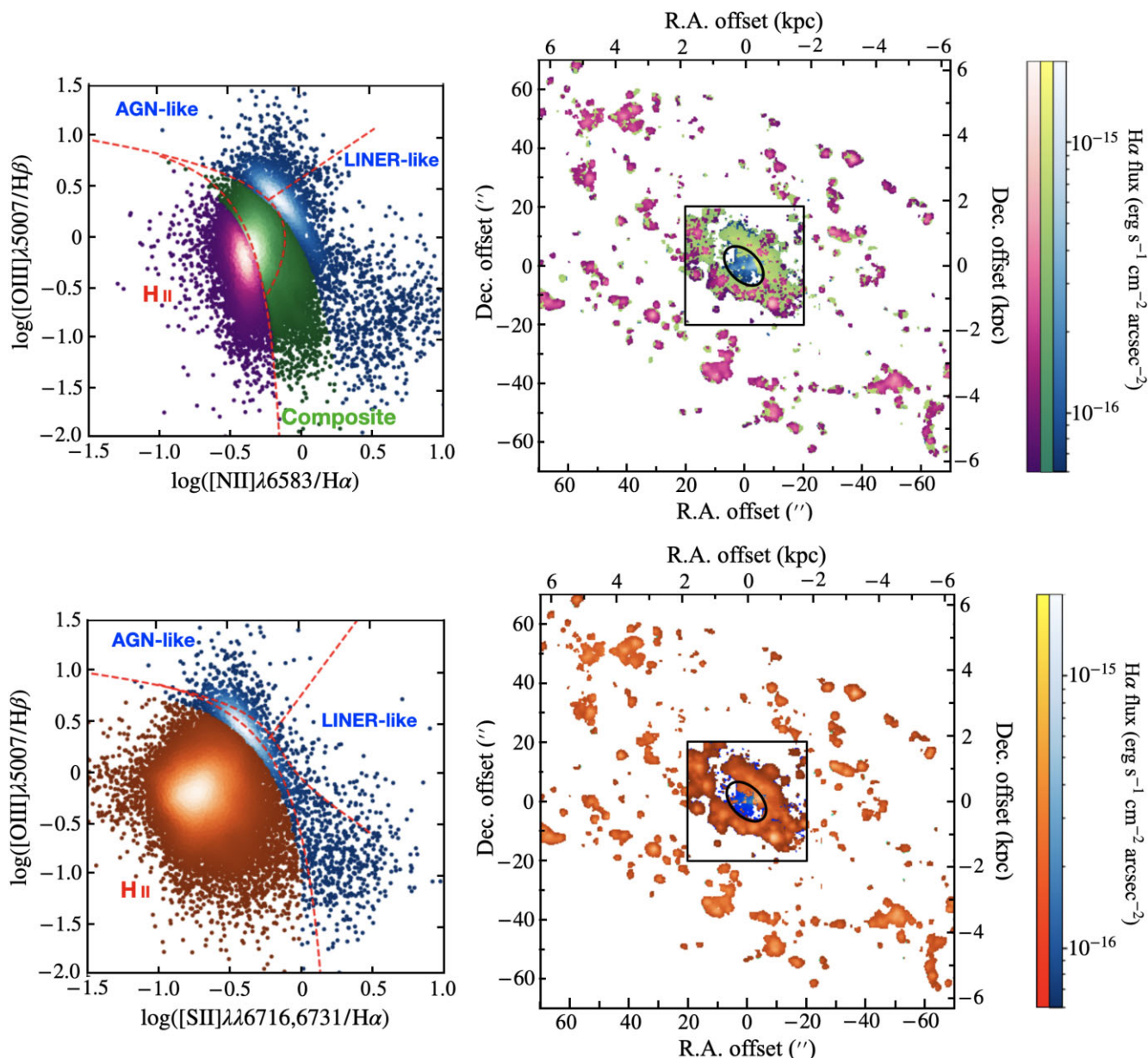


**Figure 4.** Ionization-mechanism classification over the whole disc of NGC 3169. Top left-hand panel: O3N2 diagram, showing the  $[\text{O III}]/\text{H}\beta$  versus  $[\text{N II}]/\text{H}\alpha$  line ratios. AGN/LINER-ionized (blue), H II (purple), and composite (green) regions are separated by the classification criteria of Kewley et al. (2006). The corresponding regions are colour-coded on the  $\text{H}\alpha$  flux map in the top right-hand panel, indicating the extent of the AGN impact. Bottom left-hand panel: O3S2 diagram, showing the  $[\text{O III}]/\text{H}\beta$  versus  $[\text{S II}]/\text{H}\alpha$  line ratios. AGN/LINER-ionized (blue) and H II (orange) regions are again separated by the classification criteria of Kewley et al. (2006), and the  $\text{H}\alpha$  flux map in the bottom right-hand panel is colour-coded accordingly. The classification lines of Law et al. (2021) are overlaid as red lines on the left panels, showing slightly different definitions of the regions and an additional separation of AGN- and LINER-like ionizations. The black boxes indicates the central  $\approx 3.6 \times 3.6 \text{ kpc}^2$  region, encompassing the galaxy bulge. The black ellipses separate the inner disc and outer star-forming ring discussed in Sections 4–5.

H II regions. Here, we utilize Baldwin, Phillips, and Terlevich (BPT) diagrams (Baldwin, Phillips & Terlevich 1981) to assess the extent of the AGN impact. We consider the ionized-gas emission-line ratios of  $[\text{O III}]/\text{H}\beta$ ,  $[\text{N II}]/\text{H}\alpha$  and  $[\text{S II}]/\text{H}\alpha$ . These ratios are most relevant when distinguishing H II regions from AGN-ionized regions (as described in Baldwin et al. 1981) and they are readily available from our SITELE datacubes. Fig. 4 shows two different BPT diagrams: the ‘O3N2’ diagram, which compares the  $[\text{N II}]/\text{H}\alpha$  ratios with  $[\text{O III}]/\text{H}\beta$ , and the ‘O3S2’ diagram, which compares the  $[\text{S II}]/\text{H}\alpha$  ratios with  $[\text{O III}]/\text{H}\beta$ . We applied the classification lines

of Kewley et al. (2006) to separate and thus uniquely identify H II, AGN-ionized and composite regions using the O3N2 diagram, and to separate H II and Seyfert/LINER-ionized regions using the O3S2 diagram. Spaxels are colour-coded accordingly to these ionization mechanisms in the flux maps shown in Fig. 4. The classification lines of Law et al. (2021) are overlaid on the left-hand panels of Fig. 4 for reference, as they additionally show the separation of AGN- and Seyfert-like regions.

From the O3S2 diagram, the majority of spaxels can be identified as belonging to H II regions, except within the central 650 pc radius

where only a small fraction of the spaxels contain gas definitely ionized by star formation. On the other hand, the O3N2 diagram shows more ambiguous results. While the spaxels within the central 650 pc radius also appear to be affected by AGN ionization, the composite regions are much more extended, encompassing  $\approx 50$  per cent of the spaxels in the central region and reaching beyond a radius of 2 kpc from the galaxy centre. The exact fraction of star formation ionization in these composite and AGN-ionized regions is thus unclear. Nevertheless, it is suggested from the maps that AGN-ionization occupies the diffuse emissions surrounding H $\alpha$  emission peaks.

The SFE analyses in Sections 4 and 5 thus systematically consider the three cases based on the O3N2 diagram separately. Spaxels belonging to H II regions (colour-coded purple) are referred to as star-forming regions and their SFRs can be confidently derived from their H $\alpha$  emissions. For spaxels that occupy composite regions (colour-coded green) and AGN-ionized regions (colour-coded blue), upper limits to the SFRs are estimated. The distinction between AGN-like and LINER-like ionization mechanisms is unclear, due to insufficient *S/N* of the H $\beta$  and O III lines. Nevertheless, the majority of these regions can be classified as AGN-like based on the O3S2 diagram, supporting the hypothesis that AGN photoionization is the dominant ionization mechanism within the inner 1 kpc radius of NGC 3169. However, there are also a few LINER-like regions presumably due to old stellar populations.

We also note that recent studies (e.g. Law et al. 2021) proposed using 3D diagnostic diagrams in the parameter space of [O III]/H $\beta$ , [N II]/H $\alpha$  and [S II]/H $\alpha$ , to address the difference between the O3S2 and O3N2 diagrams. We include this alternate analysis in Appendix A. As shown in Fig. A1, the nature of H II regions is confirmed while the composite regions are likely AGN ionized.

## 4 ANALYSIS: DEPLETION TIME AND GAS DYNAMICS

### 4.1 Spatially resolved depletion times

Fig. 5 shows the spatially resolved depletion time map, constructed from the ratio of the SFR and molecular gas mass surface densities ( $\tau_{\text{dep}} \equiv \Sigma_{\text{H}_2} / \Sigma_{\text{SFR}}$ ). For spaxels where both  $\Sigma_{\text{SFR}}$  and  $\Sigma_{\text{H}_2}$  are reliably measured (i.e. where both H $\alpha$  and CO are detected with *S/N* > 3),  $\tau_{\text{dep}}$  is calculated by simply dividing the two surface densities. This ratio is shown in Fig. 5 with an orange-purple colour scale. However, many spaxels have only one tracer brighter than our adopted detection threshold. When only  $\Sigma_{\text{SFR}}$  is reliably measured, we estimate a  $\tau_{\text{dep}}$  upper limit by dividing the  $3\sigma$  upper limit on the molecular gas mass surface density by the reliably measured SFR surface density, shown in Fig. 5 with a light-orange colour scale. An analogous approach is applied to spaxels where only  $\Sigma_{\text{H}_2}$  is reliably measured, to estimate a  $\tau_{\text{dep}}$  lower limit, shown in Fig. 5 with a grey-purple colour scale.

We note that Fig. 5 purposefully shows all spaxels where a tracer is detected, without distinguishing them based on the dominant ionization mechanism. For spaxels identified as composite or AGN-ionized based on their emission-line ratios (see Section 3.3), the SFR is therefore likely an upper limit. In turn, the derived depletion times measurements are likely lower limits. We return to this issue in Sections 4.2 and 4.3.

The region of NGC 3169 within the ALMA FOV has a radius of  $\approx 1.8$  kpc, and will be referred to here as the ‘central region’. It is nearly completely filled with molecular gas, while the ionized-gas emission is more patchy and concentrated within a ring-like

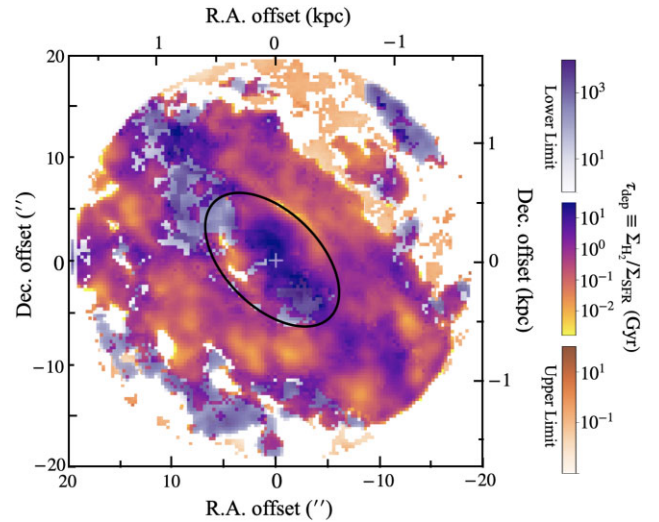


**Figure 5.** Depletion time map of the central region of NGC 3169 ( $\approx 3.6 \times 3.6$  kpc $^2$ ), encompassing the galaxy bulge, calculated from the  $\Sigma_{\text{H}_2}$  and  $\Sigma_{\text{SFR}}$  maps (see Section 4.1). The orange-purple colour scale shows actual measurements, for spaxels where both CO and H $\alpha$  are above our detection threshold. The light-orange colour scale shows upper limits, for spaxels where only H $\alpha$  is above our detection threshold. The grey-purple colour scale shows lower limits, for spaxels where only CO is above our detection threshold. Blank spaxels are either outside the ALMA field of view or have both H $\alpha$  and CO below our detection threshold. The black ellipse separates the inner disc and outer star-forming ring discussed in Sections 4–5.

structure encompassing radii of  $\approx 0.65$  kpc to  $\approx 1.8$  kpc. The average depletion time within the ring is  $\approx 0.3$  Gyr, calculated from the ratio of total molecular gas mass to total SFR. It is consistent with typical extragalactic starburst regions (e.g. Barrera-Ballesteros et al. 2021). The ring may constitute a resonance ring (e.g. Buta & Combes 1996; Buta & Purcell 1998; Comerón et al. 2014) or may simply be a pseudo-ring formed by winding spiral arms. Inside the ring (radii  $\lesssim 650$  pc), the molecular gas is more concentrated and star formation appears to be suppressed. This inner disc also has stronger impact from the bulge, with  $B/D > 1$ . The radial variation of the depletion time is discussed in Section 4.3.

### 4.2 SFR to molecular gas mass relation

Fig. 6 shows the  $\Sigma_{\text{SFR}} - \Sigma_{\text{H}_2}$  relation of all the spaxels with reliably detected H $\alpha$  and CO (orange-purple colour scale in Fig. 5). However, contrary to Fig. 5, we separate and compare the three cases discussed in Section 3.3: star-forming (orange scale), composite (green scale) and AGN-ionized (blue scale) spaxels, based on the O3N2 type BPT diagnostic described in Section 3.3. It is important to recall that for the composite and AGN-ionized cases,  $\Sigma_{\text{SFR}}$  has large uncertainties and should really be treated as an upper limit. The mean  $\Sigma_{\text{SFR}}$  and  $\Sigma_{\text{H}_2}$  within the ALMA field of view is shown with an orange star in Fig. 5. The distributions are compared to characteristic time-scales (0.1, 1, and 10 Gyr) and the power-law relations of Kennicutt (1998) and Bigiel et al. (2008), shown as light-purple and light-pink shaded areas, respectively. The power-law relation of Davis et al. (2014) for ETGs is also shown as yellow lines for reference.

Because ionized-gas and molecular gas peaks are generally not exactly co-spatial (e.g. Schruha et al. 2010; Kruijssen et al. 2019b; Schinnerer et al. 2019; Pan et al. 2022), it is common to have broad  $\Sigma_{\text{SFR}} - \Sigma_{\text{H}_2}$  distributions at sub-kpc scales. In fact, this scatter can be interpreted as a sign of a rapid cycling between gas and stars



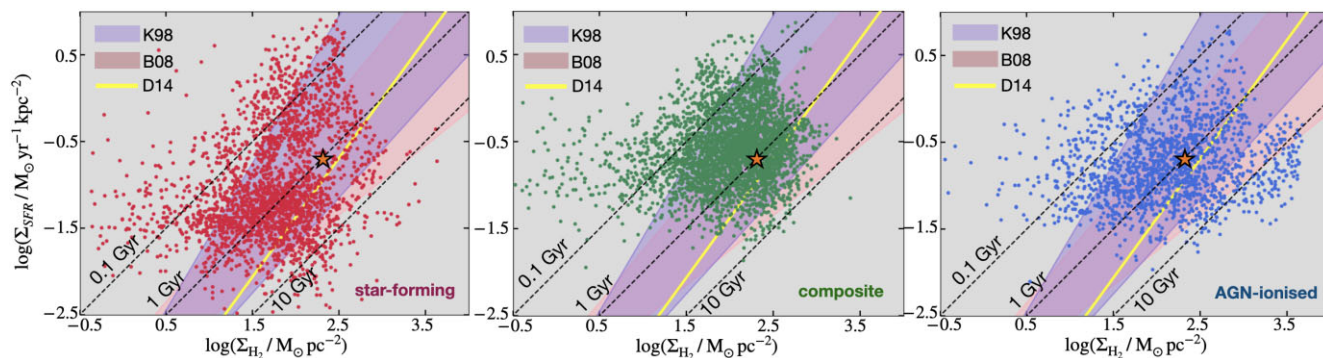


**Figure 6.** Plots of  $\Sigma_{\text{H}_2} - \Sigma_{\text{SFR}}$ , overlaid with the power-law relations of Kennicutt (1998) and Bigiel et al. (2008), shown as light-purple and light-pink shaded regions, respectively. The power-law relation of Davis et al. (2014) for ETGs is shown as a yellow line. Using the BPT analysis of Section 3.3, from the left- to right-hand panels, the panels include only spaxels classified as star-forming, composite and AGN-ionized, respectively. All data points are from spaxels with both  $\text{H}\alpha$  and CO above our detection threshold. The mean  $\Sigma_{\text{H}_2} - \Sigma_{\text{SFR}}$  of within the ALMA FOV is shown as an orange star in each panel. Representative depletion time-scales of 0.1, 1, and 10 Gyr are shown as black dashed lines.

on the sub-kpc scales, which allows us to constrain molecular gas lifetimes, as shown in Section 4.6. Fig. 6 reveals that this is indeed the case in NGC 3169, but the  $\Sigma_{\text{SFR}} - \Sigma_{\text{H}_2}$  measurements roughly follow the Kennicutt (1998) and Bigiel et al. (2008) relations in each case, encompassing depletion time-scales of 0.1 to 10 Gyr. Nevertheless, the three distributions peak at different  $\Sigma_{\text{SFR}}$  and  $\Sigma_{\text{H}_2}$ . Although some star-forming spaxels have short depletion time-scales (see left-hand panel of Fig. 6), many star-forming spaxels occupy a part of the  $\Sigma_{\text{SFR}} - \Sigma_{\text{H}_2}$  space centred at  $\Sigma_{\text{SFR}} \approx 0.04 \text{ M}_{\odot} \text{ yr}^{-1} \text{ kpc}^{-2}$  and  $\Sigma_{\text{H}_2} \approx 100 \text{ M}_{\odot} \text{ pc}^{-2}$  ( $\tau_{\text{dep}} \approx 2.5$  Gyr), slightly larger than the average  $\tau_{\text{dep}} \approx 2$  Gyr reported by Bigiel et al. (2008). In the composite regions, shown in the middle panel of Fig. 6, the distribution is centred at  $\Sigma_{\text{SFR}} \approx 0.3 \text{ M}_{\odot} \text{ yr}^{-1} \text{ kpc}^{-2}$  and  $\Sigma_{\text{H}_2} \approx 160 \text{ M}_{\odot} \text{ pc}^{-2}$  ( $\tau_{\text{dep}} \approx 0.5$  Gyr). However, this results from ionized-gas emission that is only partly due to star formation (i.e. the derived  $\Sigma_{\text{SFR}}$  of composite regions are really upper limits), so this peak would be lowered in the figure (higher  $\tau_{\text{dep}}$ ) if we knew the exact fraction of the star-forming radiation. As shown in the right-hand panel of Fig. 6, the  $\Sigma_{\text{SFR}} - \Sigma_{\text{H}_2}$  distribution of AGN-ionized regions is similar to that of composite regions, but more scattered and extended.

### 4.3 Radial trend of depletion time

Fig. 7 shows  $\tau_{\text{dep}}$  as a function of deprojected galactocentric radius, where individual spaxels are shown as purple data points, and the running mean for each case discussed in Section 3.3 is shown in the associated colour, using annuli of width 200 pc and a step size of 100 pc. Only spaxels reliably detected in both  $\text{H}\alpha$  and CO are included in this figure. For reference, the global depletion time (0.9 Gyr) is indicated by a grey horizontal line, calculated from the ratio of the total SFR to the total molecular gas mass within a radius of  $\approx 1.8$  kpc that is the ALMA FOV.

Between galactocentric radii of 0.65 and 1.8 kpc, i.e. within the previously discussed star-forming ring, the depletion times of individual spaxels cover a wide temporal range (0.03–10 Gyr). The mean  $\tau_{\text{dep}}$  within this region is  $\approx 0.3$  Gyr, lower than the global  $\tau_{\text{dep}}$  of 0.9 Gyr. Larger variations of the average depletion times occur beyond a radius of 1.8 kpc, marking the outer edge of the star formation ring. As shown in Fig. 5, GMCs and ionized-gas clouds are particularly not co-spatial beyond this radius.

Within a galactocentric radius of  $\approx 0.9$  kpc, the average  $\tau_{\text{dep}}$  rapidly increases with decreasing radius, with or without the inclusion of composite and AGN-ionized regions. For exclusively star-forming

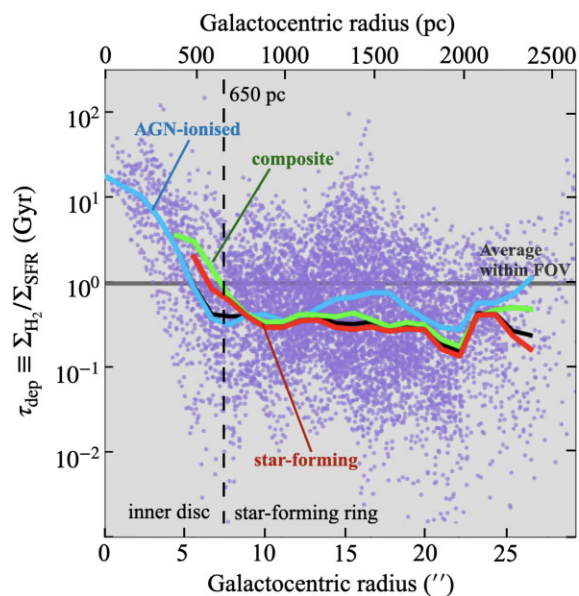


**Figure 7.** Depletion time radial profile in the central region of NGC 3169, encompassing the galaxy bulge. Purple data points are calculated from all the spaxels with both  $\text{H}\alpha$  and CO above our detection threshold in Fig. 5. The black line is the running mean of the depletion times of all data points as a function of galactocentric radius. The red, green and blue lines are the running means of the star-forming, composite and AGN-ionized regions only, respectively. The vertical black dashed line separates the inner disc and outer star-forming ring at a radius of 650 pc discussed in Sections 4–5. The grey horizontal line shows the mean depletion time within the ALMA FOV, corresponding to the orange star in Fig. 6.

regions (orange curve in Fig. 7), the mean  $\tau_{\text{dep}}$  reaches  $\approx 2.3$  Gyr at a radius of  $\approx 500$  pc. The further inclusion of composite and AGN-ionized regions (blue curve) is considered merely for illustration purposes, but clearly shows that there is  $\text{H}\alpha$  emission down to a radius of  $\approx 100$  pc, partly as the result of AGN ionization. The measurements nevertheless clearly indicate depletion times of at least the age of the Universe (most likely more) in the central few hundred parsecs. Therefore, although the average  $\Sigma_{\text{SFR}}$  and  $\Sigma_{\text{H}_2}$  of this central region follows the SF relations of star-forming regions, we observe a clear transition from efficient SF in the star-forming ring to quenched SF within the central  $\approx 500$  pc in radius. These low SFEs result from

feeble star formation in that region, despite plentiful molecular gas, potentially due to accretion on to the central regions.

The radial extent of AGN ionization is also illustrated in Fig. 7. While H $\alpha$  emissions reaches the centre of the galaxy, the inner 400 pc in radius are dominated by AGN ionization. Individual spaxels that are confidently classified as exclusively star-forming are located at a galactocentric radius of at least 650 pc. The size of the AGN-ionized region is consistent with that of other nearby galaxies. For example, it is within the broad range of 0.3–10 kpc reported by Chen et al. (2019) based on 152 AGN-host galaxies using the Mapping Nearby Galaxies at Apache Point Observatory (MaNGA) survey.

#### 4.4 Virial parameters

To take a more in-depth look at the star formation on cloud scales, we identified H II regions using the SITELLE H $\alpha$  data and algorithms developed by Rousseau-Nepton et al. (2018), summarized below. The H $\alpha$  flux peaks are first identified, based on the following criteria: (1) the flux of the peak spaxel is greater than the flux of at least five immediately surrounding spaxels, (2) the total flux in a  $3 \times 3$  spaxels box centred on the emission peak is above the  $3\sigma$  detection threshold and (3) if two emission peaks are separated by a distance smaller than the seeing ( $1''.1$  or 99 pc in this case), only the brightest peak is preserved. Given an estimate of the characteristic radius of H II regions, spaxels are then classified into zones surrounding the peaks, and the boundaries of the spatial zones are defined. Fig. B1 in Appendix B shows these peaks and region boundaries overlaid on the H $\alpha$  flux map of NGC 3169. For each H II region, a 2D Gaussian fit is then carried out and the luminosity ( $L_{\text{H II}}$  based on H $\alpha$  flux) and size (half-width at half-maximum  $R_{\text{H II}}$ ) of the best-fitting Gaussian are calculated (and taken as those of the H II region). Furthermore, the spectra from the SITELLE H $\alpha$  datacube are binned around the best-fitting peak of each H II region, according to the size of the region, and the resulting spectrum is fit with ORCS to derive the velocity dispersion ( $\sigma_{\text{H II}}$ ) of the region. We note that not all H II regions identified are necessarily also star-forming regions, as some may be partially or primarily ionized by the AGN. The full H II region catalogue is presented in Table B1 in Appendix B.

Based on these measurements, the virial parameter of each region is calculated as

$$\alpha_{\text{vir, H II}} \equiv 5 \frac{\sigma_{\text{H II}}^2 R_{\text{H II}}}{G M_{\text{H II}}} \quad (8)$$

(Bertoldi & McKee 1992), where  $M_{\text{H II}}$  is the ionized-gas mass of the region, estimated from

$$\frac{M_{\text{H II}}}{M_{\odot}} = 1.57 \times 10^{-17} \left( \frac{L_{\text{H II}}}{\text{erg s}^{-1}} \right)^{\frac{1}{2}} \left( \frac{R_{\text{H II}}}{\text{pc}} \right)^{\frac{3}{2}} \quad (9)$$

(Zaragoza-Cardiel et al. 2015). This ionized-gas mass assumes that the mean electron number volume density can be derived from  $L_{\text{H II}}$  assuming a spherical geometry, and that all ionizing photons are from hot/massive stars.

As the ionized-gas mass is usually only a fraction of the total gas mass (Zaragoza-Cardiel et al. 2015), the virial parameter calculated above is typically larger than that based on molecular gas. Therefore, it is not fair to use a criterion of about unity to diagnose whether a cloud is gravitationally bound (often stated as  $\alpha_{\text{vir}} \lesssim 2$ ). However, it is meaningful to compare virial parameters measured for different H II regions. A larger virial parameter implies a higher kinetic energy that is harder to counter-balance with gravity and is more likely to require external pressure to maintain equilibrium. As should then be expected, there is a weak correlation between  $\alpha_{\text{vir, H II}}$  and  $\tau_{\text{dep}}$ ,

shown in the left-panel panel of Fig. 8. The  $\tau_{\text{dep}}$  in each H II region is calculated based on the ratio of molecular gas mass and SFR within the region. According to equations (8), variations of  $\alpha_{\text{vir, H II}}$  are in fact primarily due to the velocity dispersions. This suggests that large  $\tau_{\text{dep}}$  in the inner 1-kpc radius can be associated with high turbulence.

As a comparison, we also estimate the molecular gas virial parameter on the cloud scale, which is equivalent to the CO spaxel size of  $\approx 35$  pc. The molecular gas virial parameter ( $\alpha_{\text{vir, H}_2}$ ) can be calculated following the method from Rosolowsky & Leroy (2006) that is recently adopted by Sun et al. (2020):

$$\alpha_{\text{vir, H}_2} = 3.1 \times \left( \frac{\Sigma_{\text{H}_2}}{10^2 M_{\odot} \text{ pc}^{-2}} \right)^{-1} \left( \frac{\sigma_{\text{H}_2}}{10 \text{ km s}^{-1}} \right)^2 \left( \frac{D_{\text{spaxel}}}{150 \text{ pc}} \right), \quad (10)$$

where  $\Sigma_{\text{H}_2}$  is calculated in Section 3.2,  $\sigma_{\text{H}_2}$  is taken from the moment-2 map shown in Fig. 3 and  $D_{\text{spaxel}}$  is the CO spaxel size of  $\approx 35$  pc, comparable to typical GMC sizes. As shown in the right-hand panel of Fig. 8 with orange data points and associated red distribution density contours, the majority of spaxels belonging to star-forming regions appear to be roughly virialized, with virial parameters varying between 0 and 10 and depletion times less than 1 Gyr. A virial parameter equals 2 is shown with a vertical dotted line on the right-hand panel of Fig. 8, for illustration purposes. On the other hand, a wider range of  $\alpha_{\text{vir, gas}} - \tau_{\text{dep}}$  parameter space is covered by all reliably measured spaxels (i.e. including those with composite and AGN ionization), shown with grey data points and associated black distribution density contours in the right-hand panel of Fig. 8. This suggests that AGN-ionization increases both  $\alpha_{\text{vir, gas}}$  and  $\tau_{\text{dep}}$ . However, none of the mean molecular mass surface density, velocity dispersion and/or size is accurately estimated from that within a single spaxel, so the virial parameters evaluated using equation (10) should not be taken nor interpreted literally. Instead, they are rough indicators of the significance of the kinetic energy (turbulence) relative to the gravitational potential (gravity), which varies among spaxels.

#### 4.5 Non-circular motions

We now probe both molecular gas and ionized gas kinematics in the central region of NGC 3169, to understand more about the SFEs in the inner disc and the star-forming ring.

For the molecular gas, we use the 3DBAROLO software<sup>1</sup> of Teodoro & Fraternali (2015), which fits tilted-ring models to 3D emission-line datacubes, taking advantage of the high spectral and spatial resolutions of the ALMA CO observations. Following a first fit with all parameters free, we fix the dynamical centre (spatially and spectrally) and inclination, while letting the position angle (PA) vary to account for the warping of the disc. The rotation and radial velocities from the resulting best-fitting model are shown in Fig. 9 with blue lines. As a reference, the corresponding position–velocity (PV) profile and best-fitting results of all the relevant parameters are in Appendix C.

We use another method to determine the rotation and radial velocity profiles of the ionized gas, by performing Markov chain Monte Carlo (MCMC) fits of the tangential and radial velocity components. A nuisance parameter is also applied, which corresponds to the line-of-sight velocity scatter in the axisymmetric modelling of the observed asymmetric kinematics. The Bayesian inferences are done using the Python library EMCEE (Foreman-Mackey et al. 2013), fixing the dynamical centre, inclination and PA of the H $\alpha$  velocity field

<sup>1</sup><https://editeodoro.github.io/Bbarolo/>

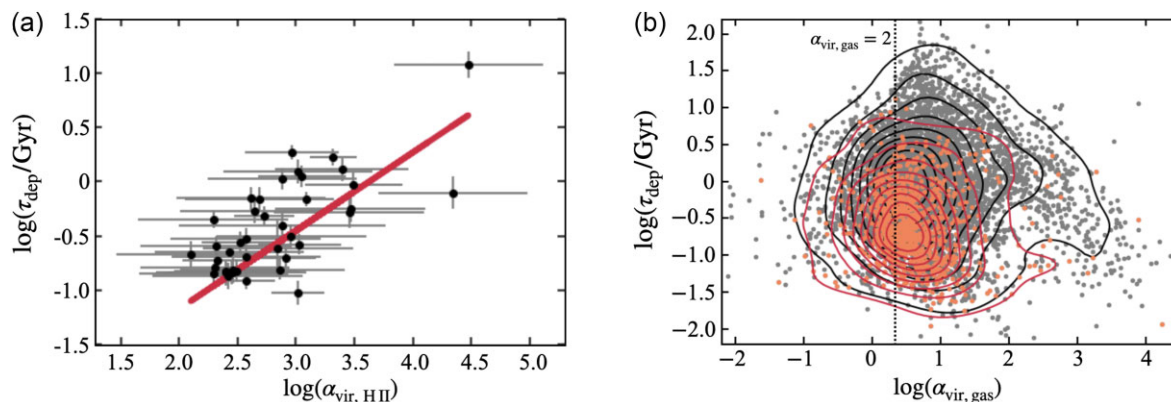


**Figure 8.** Panel (a): H II region depletion time versus virial parameter, with the best-fitting power-law relation overlaid as a red line. Panel (b): depletion time versus virial parameter calculated from the molecular gas at each spaxel. The orange data points and associated red density contours are based on spaxels classified as star-forming only, while the grey data points and associated black density contours are based on all the spaxels with reliable measurements of  $\tau_{\text{dep}}$  and  $\alpha_{\text{vir, gas}}$ .

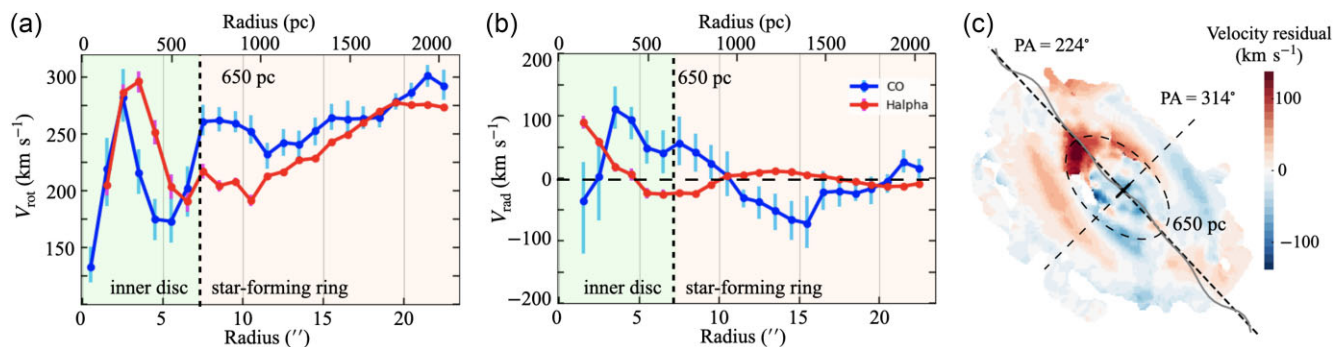


**Figure 9.** Panel (a): rotation curve (left-hand panel) and radial velocity profile (right-hand panel) for both CO (blue line) and H $\alpha$  (red line) gas. The green and orange backgrounds are separated at the dotted black line, indicating a radius of 650 pc that is the intersection of the inner disc and the star-forming ring. Panel (b): CO velocity residual map, defined as the difference between the observed velocity, shown in Fig. 3(b), and the best-fitting circular velocity model from 3DBarolo.

as the best-fitting values obtained from the 3D Barolo for the CO gas. This way, we use the same set of kinematic parameters for both gaseous components to assist the comparisons, while taking into account the individual errors on the line-of-sight H $\alpha$  velocities, which are unique to the SITELLE datacubes. The best-fitting rotation and radial velocities are shown in Fig. 9 with red lines.

The rotation and RV profiles of CO and H $\alpha$  gas show different behaviours within the inner disc and in the star-forming ring, marked in Fig. 9 with green and orange-shaded areas, respectively. The inner edge of the star-forming ring at 650 pc radius is marked with a black-dotted line. Beyond the radius of  $\approx 650$  pc, the derived rotation curve of CO gas suggests roughly constant rotation velocities of 240–260 km s $^{-1}$  in the star-forming ring. The rotation curve of H $\alpha$  gas, however, increases from 200 km s $^{-1}$  at 650 pc to 280 km s $^{-1}$  at 1700 pc.

Higher CO rotation velocities are found in many galaxies (Davis et al. 2013; Levy et al. 2018). If H $\alpha$  is tracing recent star formation, it would typically co-rotate with CO gas in the mid-plane of the galaxy disc. The discrepancy in NGC 3169 can be explained by a different scale height of molecular and ionized gas, due to the fact that the H $\alpha$  gas is associated with a mixture of ionization mechanisms, including old stellar population and shock-ionization from the AGN. Based on our ionized gas emission-line ratio analysis in Section 3.3, this is likely the case. The positive slope of H $\alpha$  rotation velocities from

inner parts of the star-forming ring to outer parts, where they merge with CO rotation velocities, also indicates that the fraction of recent star-forming ionization is dominant as we move away from the centre of the galaxy.

The kinematics in the inner disc appear to be much more complex. Both CO and H $\alpha$  rotation velocities rise to  $\approx 300$  km s $^{-1}$  and then rapidly drop to below 200 km s $^{-1}$ . The resulting rotation curve resembles those of many barred galaxies, with a characteristic ‘double-hump’ (i.e. a steep inner rise of the rotation velocities, followed by a decrease and local minimum before a second increase to the flat part of the rotation curve; e.g. Athanassoula & Bureau 1999; Bureau & Freeman 1999). Although NGC 3169 does not harbour a large-scale bar, Figs 1 and 3 suggest a small-scale bar within the star-forming ring (half-length  $\lesssim 650$  pc). This structure may be responsible for transporting material to the inner regions, causing high turbulence.

As shown in the middle panel of Fig. 9, the radial velocities of the CO and H $\alpha$  gas oscillate from positive to negative, tracing expansion and contraction at different locations. In particular, the oscillations of CO and H $\alpha$  are out of phase, indicating complex non-circular motions. The right-hand panel of Fig. 9 shows the residual velocity of CO gas, which is the difference between the observed velocity (as shown in Fig. 3) and the best-fitting model from 3DBarolo. It shows the presence of significant spiral



arm-like residuals. Given the presence of a small-scale bar, such residuals may trace inflow/outflow streaming motions induced by the inner bar (see e.g. Domínguez-Fernández et al. 2020; Ruffa et al. 2022). Another source of non-circular motion is outflows. In Fig. 9(c), there appear to be particularly large CO residual velocities near the intersection of the major axis and the 650 pc line. At this location, we also find secondary emission peaks on the CO spectra, as well as asymmetric broadening of ionized gas emission lines. As these features are close to the galaxy centre, they suggest the presence of gas blobs ejected from the galaxy plane, as a result of AGN-driven outflows. However, the signal-to-noise ratio at this location is not robust enough to draw concrete conclusions.

Regardless of the sources of non-circular motions, high-velocity dispersions are observed within the inner disc as a result. As shown in Fig. C1, the molecular gas velocity dispersions are high throughout ( $\sigma_{\text{gas}} \gtrsim 20 \text{ km s}^{-1}$ ) and rise rapidly with decreasing radius within the inner disc, reaching  $\approx 70 \text{ km s}^{-1}$  in the very centre. Since 3DBAROLO takes into consideration beam smearing effects, the best-fitting velocity dispersion result can assist the moment-2 maps in Fig. 3 to illustrate the turbulent gas motions within the inner region of NGC 3169.

#### 4.6 Molecular cloud time-scales

A spatial de-correlation between CO and H $\alpha$  emission regions is commonly observed in nearby galaxies (e.g. Kruijssen et al. 2019b; Chevance et al. 2020; Zabel et al. 2020), due to the different life cycles of different regions (e.g. Kruijssen & Longmore 2014), i.e. at least partially independent cloud assembly, collapse, star formation and disruption due to stellar feedback. A statistical analysis of CO and H $\alpha$  snapshots of these regions therefore allows us to estimate the characteristic lifetime of the molecular gas ( $t_{\text{gas}}$ ), the duration of the young stellar phase ( $t_{\text{star}}$ ), duration of the overlapping/feedback phase ( $t_{\text{fb}}$ ), as well as the characteristic separation length of individual regions ( $\lambda$ ). To infer these quantities, we adopt here the methods developed by Kruijssen et al. (2018) and use the associated HEISENBERG code. This approach has been used previously to characterise the GMC life-cycle for a wide range of observed galaxies (e.g. Kruijssen et al. 2019b; Chevance et al. 2020, 2022; Ward et al. 2020; Zabel et al. 2020; Kim et al. 2021), as well as for numerical simulations (e.g. Fujimoto et al. 2019; Jeffreson et al. 2021).

We briefly summarize the methodology below, while the details can be found in section 3 of Kruijssen et al. (2018). The first step is to measure CO-to-H $\alpha$  flux ratios in apertures of a range of sizes, all centred on the peaks of the CO and the H $\alpha$  emission, respectively. The identification of the molecular gas and ionized-gas peaks and the total flux calculations use the same maps as for the depletion time calculations (see Section 4). The relative changes of the flux ratios compared to the galactic average, as a function of the aperture size, are governed by the three aforementioned time-scales ( $t_{\text{gas}}$ ,  $t_{\text{star}}$ , and  $t_{\text{fb}}$ ) as well as  $\lambda$ , as shown in Kruijssen & Longmore (2014). We fit the observed CO-to-H $\alpha$  flux ratio with the analytical model presented in Kruijssen et al. (2018) to constrain  $\lambda$  and the ratios  $t_{\text{gas}}/t_{\text{star}}$  and  $t_{\text{fb}}/t_{\text{star}}$ . Assuming a reference time-scale  $t_{\text{star, ref}} = 4.3 \text{ Myr}$  for the isolated stellar phase (the appropriate time-scale when using continuum-subtracted H $\alpha$  emission as the SFR tracer; see Haydon et al. 2020), we convert these time-scale ratios into absolute values.

As the input maps for this analysis require contiguous emission across each region, a naive separation of star-forming and AGN-ionized regions based on BPT diagram diagnostics would not work. Considering this constraint, we adopt a different approach to nevertheless attempt to distinguish emission arising from each of the three ionization mechanisms discussed in Section 4 (i.e. star-forming,

**Table 2.** Best-fitting time-scales and separation length.

|                         | Case A              | Case B               | Case C               |
|-------------------------|---------------------|----------------------|----------------------|
| $t_{\text{gas}}$ (Myr)  | $7.1^{+5.3}_{-2.1}$ | $10.5^{+4.2}_{-2.6}$ | $6.7^{+5.0}_{-1.4}$  |
| $t_{\text{fb}}$ (Myr)   | $\leq 2.9$          | $\leq 3.3$           | $\leq 1.5$           |
| $t_{\text{star}}$ (Myr) | $5.5^{+1.5}_{-0.9}$ | $5.9^{+1.7}_{-0.9}$  | $4.4^{+1.4}_{-0.16}$ |
| $\lambda$ (pc)          | $145^{+59}_{-38}$   | $148^{+53}_{-28}$    | $163^{+33}_{-21}$    |

*Note.* All values are associated with their  $1\sigma$  uncertainties

composite and AGN-ionized regions). For Case A listed in Table 2, all emission within the field of view is considered, implying that all three ionization mechanisms are included. For Case B, a central region of 650 pc radius is masked out. As the majority of AGN-ionized regions is within this central region, Case B includes mostly star-forming and composite regions. For Case C, in addition to removing the central region, diffuse emissions is also removed across the field, achieved by tapering large-scale emission in Fourier space. More specifically, the emission in each line is transformed into Fourier space, and a Gaussian high-pass filter is then applied centred at zero Fourier frequency, using the best-fitting  $\lambda$  (the separation length-scale) in an iterative process (Hygate et al. 2019). As can be inferred from Fig. 4 and the discussions in Sections 3.3 and 5.2, diffuse emission is dominated by ionization from the AGN, generally leading to a composite classification. Case C thus mostly contains star-forming regions, as required by the adopted methodology, and therefore constitutes our reference case. The Case C maps, relative flux ratios and best-fitting model from the HEISENBERG code are shown in Fig. 10, while those for Cases A and B are shown in Fig. D1 for reference.

As listed in Table 2, the fitting results from the three cases agree with one another within the  $1\sigma$  uncertainties. The fact that the separation lengths are 1.5 times larger than the spatial resolution of our data (i.e.  $\lambda > 100 \text{ pc}$ ) gives us confidence that the spatial resolution of our maps is sufficient for this analysis. The separation length of  $\approx 160 \text{ pc}$  is also typical of nearby spirals (100–300 pc; Chevance et al. 2020). The molecular gas lifetime is rather short ( $t_{\text{gas}} = 6.7^{+5.0}_{-1.4} \text{ Myr}$ ), but with a high upper limit. A gas lifetime of  $\approx 10 \text{ Myr}$ , comparable to the representative cloud free-fall time, typically indicates that the cloud is regulated by internal dynamical processes. Comparing to the GMC lifetimes of other nearby galaxies (e.g. Kruijssen et al. 2019b; Zabel et al. 2020; Chevance et al. 2022), the cloud lifetime is reasonable, given the small galactocentric radii where the dynamical time-scales are typically small. However, the number of flux peaks identified, 77 for CO flux and 80 for H $\alpha$  flux, is not large enough to constrain time-scale radial trends. The blending of the CO and H $\alpha$  peaks also results in significant uncertainties on the feedback time-scale  $t_{\text{fb}}$ . This is characterized with a region filling factor  $\zeta$  described in Kruijssen et al. (2018), which is  $\approx 0.7$  in our best-fitting result that prevents the accurate measurement of  $t_{\text{fb}}$  within a few Myr (see e.g. Chevance et al. 2022). Therefore, only the upper limits of  $t_{\text{fb}}$  for each case are listed in Table 2. These factors unfortunately prohibit firm conclusions about the nature of the dominant GMC-scale feedback and quenching mechanisms in the central region of NGC 3169. Observations with higher spatial resolution and larger FOV can help to resolve some of the issues.

## 5 DISCUSSION

### 5.1 Quenching from bulge dynamics

In Section 4.3, we showed that the short depletion times in the star-forming ring gradually increase as we probe close to the centre of

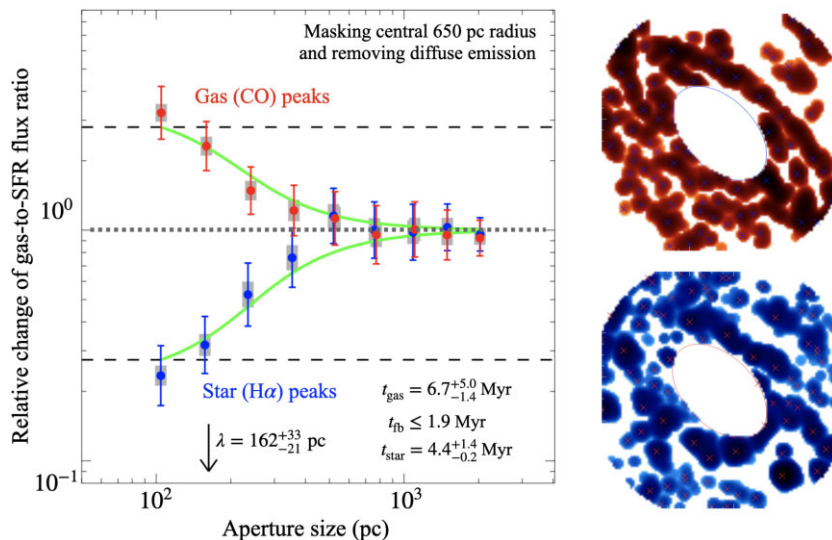


**Figure 10.** Left-hand panel: relative change of the CO-to-H $\alpha$  flux ratio as a function of aperture size for Case C (see Section 4.6, with a focus on the molecular gas peaks (red data points) and the ionized-gas peaks (blue data points)). The best-fitting model based on the uncertainty principle for star formation of Kruijssen et al. (2018) is shown as a green solid line (see Section 4.6). The horizontal grey dotted line indicates the galactic average of the flux ratio normalized to the mean  $\tau_{\text{dep}} = 0.9$  Gyr within the ALMA FOV. The associated best-fitting parameters with  $1\sigma$  uncertainties are listed at the bottom of the panel. Right-hand panel: corresponding CO (top panel) and H $\alpha$  (bottom panel) maps.

the galaxy, and identified it as a quench of star formation. A common explanation for star formation quenching in galaxy bulges is the bulge dynamics itself, which can enhance velocity dispersions in the central regions of the galaxy (e.g. Martig et al. 2009, 2013). In particular, Gensior et al. (2020) and Gensior & Kruijssen (2021) simulated the influence of a bulge on the radial variations of the SFE. A power-law relation normally exists between  $\Sigma_{\text{SFR}}$  and  $\Sigma_{\text{H}_2}$  in bulgeless galaxies (i.e. the usual ‘spatially resolved’ Kennicutt–Schmidt relation; Bigiel et al. 2008; Kennicutt & Evans 2012). A similar power-law relation is reproduced by the simulations of bulgeless galaxies in Gensior et al. (2020), but with a different slope. However, adding bulges to the galaxy models results in  $\Sigma_{\text{SFR}}/\Sigma_{\text{H}_2}$  ratios that are systematically lower at small galactocentric radii, and the decrease is more extreme in denser bulges.

Here, we attempt to compare the radial trend of  $\Sigma_{\text{SFR}}/\Sigma_{\text{H}_2}$  of both our NGC 3169 data and simulations of galaxies with dense bulges. The  $\Sigma_{\text{SFR}}-\Sigma_{\text{H}_2}$  ratio of NGC 3169 is shown in Fig. 11 as a function of galactocentric radius (using running means; another way to visualize Figs 5–7). The estimated power-law relation of bulgeless galaxies from the simulation of Gensior et al. (2020) is shown as a red dashed line, and representative depletion time-scales shown as black dashed lines. The bulge simulations of Gensior & Kruijssen (2021), with an effective radius of  $\approx 1$  kpc and a bulge-to-total mass ratio of  $\approx 0.9$ , are shown with triangles. As the simulations are idealized cases, with smooth rotation curves and a limited range of  $\Sigma_{\text{H}_2}$ , they do not accurately represent the bulge environment of NGC 3169. Nevertheless, the simulations do show that the presence of a bulge can produce a radial trend of the  $\Sigma_{\text{SFR}}/\Sigma_{\text{H}_2}$  ratio similar to that observed in NGC 3169. We also notice that the simulated bulges are much denser than the bulge of NGC 3169, with an effective radius  $\approx 1.4$  kpc, a bulge-to-total mass ratio  $\approx 0.1$  and B/D  $> 1$  only within a radius of 660 pc. This suggests that other mechanisms may be required to quench SF within the central kpc of this galaxy.

Using the relation found by Gensior & Kruijssen (2021), the sSFR predicted from bulge dynamics can be inferred by relating it to the total molecular gas-to-stellar mass fraction ( $f_{\text{gas}}$ ) and the stellar mass

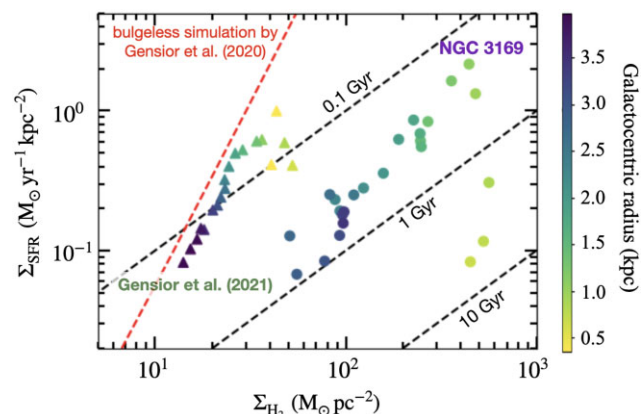


**Figure 11.** Relation of  $\Sigma_{\text{H}_2}-\Sigma_{\text{SFR}}$ . The galactocentric radius of each data point is indicated by its colour scales. Filled circles are azimuthal averages from our NGC 3169 data, for spaxels classified as star-forming only. Filled triangles are azimuthal averages from the simulations of Gensior & Kruijssen (2021). The red dashed line shows the power-law relation best fitting the results from a bulgeless galaxy simulation (Gensior et al. 2020). Representative depletion time-scales of 0.1, 1, and 10 Gyr are shown as black dashed lines.

surface density ( $\mu_*$ ):

$$\log(\text{sSFR}_{\text{sim}} / \text{Gyr}^{-1}) = -1.79 + 4.00 \log\left(\frac{f_{\text{gas}}}{0.05}\right) - 0.99 \log\left(\frac{\mu_*}{10^8 \text{ M}_\odot \text{ kpc}^{-2}}\right). \quad (11)$$

Using the total molecular gas mass of  $\approx 10^{9.3} \text{ M}_\odot$ , the total stellar mass of  $\approx 10^{10.8} \text{ M}_\odot$  and the stellar surface density of  $\approx 10^{8.3} \text{ M}_\odot \text{ kpc}^{-2}$  (all listed in Table 1), we obtained a prediction of  $\log(\text{sSFR}_{\text{sim}} / \text{Gyr}^{-1}) = -0.68$ . Comparing to the observed  $\log(\text{sSFR}[\text{Gyr}^{-1}]) = -1.55$ , using the total SFR of  $\approx 10^{0.29} \text{ M}_\odot \text{ yr}^{-1}$  (in Table 1), this suggests that bulge dynamics are not the sole source

of SF suppression. Other factors could be acting in concert with the dynamics to further decrease the sSFR.

## 5.2 AGN feedback

In Section 3.3, with the aid of BPT diagrams, we analysed the optical emission-line ratios, across the whole disc of NGC 3169. In addition to using these to separate star formation, composite and AGN ionization, which help to interpret the (often large) inferred molecular gas depletion times, we established that AGN ionization is pervasive up to a galactocentric radius of  $\approx 2$  kpc. It is therefore natural to investigate whether other lines of evidence support a causal relationship between the LLAGN and SFE.

One important observable is the coincidence of a large velocity dispersion (in both ionized and molecular gas) and AGN ionization in many spaxels. Indeed, as shown in Figs 2 and 3, the velocity dispersions of both H $\alpha$  and CO are significantly larger in the inner disc than in the star-forming ring (i.e. at radii  $\lesssim 650$  pc), while Fig. 4 clearly shows that these same regions are AGN ionized, potentially indicating shock heating and/or ionization from the AGN radiation. We can further probe this velocity dispersion–ionization mechanism correlation with star formation quenching by looking back at the H II region dynamics discussed in Section 4.4. There, we uncovered a weak correlation between the H II regions’ virial parameters and the molecular gas depletion times, higher virial parameters being associated with longer depletion times (or equivalently lower SFEs). As the velocity dispersion is the dominant parameter in virial parameter calculations, there is in turn a correlation between these high-velocity dispersions and suppressed star formation. However, it is important to note that beam smearing may have a large impact here due to the rapid changes of rotation curve slopes shown in Section 4.5.

As discussed in Sections 2.3 and 4.5, there are traces of AGN-driven outflows that can contribute to the enhanced velocity dispersions discussed above, quenching the star formation in the innermost regions of NGC 3169. Similar negative feedback mechanisms are discussed in recent works of Venturi et al. (2021) and Gao et al. (2021). On the other hand, we also identified a fraction of AGN-ionization in the star-forming ring, associated with diffuse emissions surrounding the H $\alpha$  peaks (see Section 3.3). It suggests positive feedback from the AGN that enhanced SF in the star-forming ring. Overall, AGN feedback could thus be partly responsible for the radial profile of SFE from the star-forming ring to the central 100 pc in radius of NGC 3169.

## 5.3 Quenching from the bar

As shown in Section 4.5, there are multiple sources of non-circular motions in the central region of NGC 3169. An outstanding one is significant spiral-like structures that can be associated with inflow/outflow streaming motions as a result of the small-scale bar. Barred galaxies often have characteristic star formation features, as studied in great details in the recent work of Sato et al. (2021). In particular, there are often cold gas overdensities and enhanced star formation both in a nuclear ring, caused by resonances with the bar, and at the nodes where the spiral arms and bar connect. With material transported into the bulge by inflows within the bar, turbulence can be enhanced in the central region and star formation may be suppressed. However, simulations of clouds and star formation in galactic bars (e.g. Renaud et al. 2015) have also shown that enhanced turbulence can, in some cases, induce strong local compression and lead to starbursts. These simulations

also illustrated that strong shear along the elongated orbits in galactic bars may instead suppresses turbulence and the associated local compression, while also stabilizing against gravitational instabilities.

The presence of the small-scale bar may explain the radial trend of  $\tau_{\text{dep}}$  observed in NGC 3169, although there is no corresponding overdensity of GMCs at the nodes. We should also note that the velocity dispersions of both the ionized and the molecular gas in NGC 3169 are not particularly high. As illustrated in many works (e.g. Sun et al. 2020; Deconto-Machado et al. 2022), in the central kpc in radius, AGN-host galaxies can have velocity dispersions over  $100 \text{ km s}^{-1}$  higher than those of other galaxies with similar morphologies.

A more detailed analysis of the spatially resolved properties of GMCs in NGC 3169 could also provide more information about the influence of the bulge dynamics and shear. For example, as part of the WISDOM project, Liu et al. (2021) analysed individual GMCs in NGC 4429 and revisited the conventional Virial theorem, including the effects of the galactic gravitational potential in addition to the usual cloud self-gravity. Applying such a model to the bulge region of NGC 3169 may help to better understand the dynamics of individual GMCs and H II regions, and to examine the impact of energy injection from the AGN. However, the nominal spatial resolution of the current CO observations ( $\approx 65$  pc) is not sufficient for this purpose. It may still be worthwhile to probe giant molecular associations (GMAs; i.e. collections of GMCs), but wider spatial coverage would be necessary to draw firm statistical conclusions.

## 6 CONCLUSIONS

In this work, we study the SFE of the central region of NGC 3169 ( $\approx 3.6 \times 3.6 \text{ kpc}^2$ ). The molecular gas is traced by  $^{12}\text{CO}(2-1)$  observations from ALMA, while the SFR is traced by extinction-corrected H $\alpha$  observations from SITELLE at CFHT. The surface densities of molecular and ionized gas are measured at a spatial resolution of  $< 100$  pc. The depletion times and  $\Sigma_{\text{SFR}}-\Sigma_{\text{H}_2}$  relation are measured accordingly and probed for variations with galactocentric distance and bulge dynamics. To explain the enhanced star formation suppression closer to the galactic centre, we examined the potential impact of AGN feedback and other mechanisms. Our key findings are summarized as follows:

(i) We identified star-forming, AGN-ionized, and composite regions based on emission-line ratios, and showed that the AGN impact is strongest within the inner disc, while composite regions reach over 2 kpc from the galaxy centre. For the AGN-ionized and composite regions, we estimated upper limits of  $\Sigma_{\text{SFR}}$  and hence lower limits of depletion times.

(ii) The overall star formation relation follows closely the power-law relations of Kennicutt (1998) and Bigiel et al. (2008), with depletion times ranging from 0.1 to 10 Gyr. For star-forming regions, the peak of  $\Sigma_{\text{SFR}}-\Sigma_{\text{H}_2}$  distribution is slightly above 2 Gyr, indicating star formation quenching. For composite and AGN-ionized regions, the distributions have different peaks with much larger  $\Sigma_{\text{SFR}}$  and slightly larger  $\Sigma_{\text{H}_2}$ , which could however result from  $\Sigma_{\text{SFR}}$  overestimates due to the unknown fraction of star-forming ionization in these spaxels.

(iii) Ionized-gas emission appears to be concentrated within a star-forming ring, while molecular gas fills up both a smaller central disc and the ring. The depletion times in the star-forming ring are  $\approx 0.3$  Gyr, comparable to typical starbursts. As the radius decreases within a galactocentric distance of  $\approx 0.9$  kpc, star formation becomes scarce while molecular gas gets denser, resulting in a longer depletion



time. In star-forming regions,  $\tau_{\text{dep}}$  increases gradually from  $\approx 0.3$  Gyr in the starburst ring to  $\approx 2.3$  Gyr at a radius of 500 pc.

(iv) There is a weak correlation between the molecular gas depletion times and the virial parameters of the associated H II regions. As large virial parameters are generally associated with high velocity dispersions, this suggests that the SFEs in the bulge of NGC 3169 are affected by turbulence. Potential sources of turbulence in this region are outflows from the AGN and inflows from the spiral arms to the inner bar. The molecular gas lifetime and feedback durations are constrained by the uncertainty principle for star formation of Kruijssen et al. (2018) are reasonable comparing to other nearby galaxies. Bulge dynamics may also contribute to the star formation quenching in the central region.

Spatially resolved analyses of GMCs and H II regions are underway to better understand the kinematics and local environments of the bulge of NGC 3169 and similar galaxies. We are also exploiting other SFR indicators such as free-free emission from VLA, to minimize any uncertainty caused by dust extinction. Most importantly, to piece together the puzzle of star formation quenching at the heart of galaxies, we require more observational data probing galaxy bulges and ETGs.

## ACKNOWLEDGEMENTS

We thank the referee, Frederic Bournaud, for useful comments that improved the analyses and manuscript. We thank Federico Lelli for the help with `3DBAROLO` and valuable discussions. This research is based on observations obtained with the SHELLE instrument on the Canada-France-Hawaii Telescope (CFHT) which is operated from the summit of Maunakea, and the Atacama Large Millimeter/submillimeter Array (ALMA) in the Atacama desert. This paper makes use of the following ALMA data: ADS/JAO.ALMA#2015.1.00598.S, ADS/JAO.ALMA#2016.2.00053.S. ALMA is a partnership of ESO (representing its member states), NSF (USA) and NINS (Japan), together with NRC (Canada), MOST and ASIAA (Taiwan), and KASI (Republic of Korea), in cooperation with the Republic of Chile. The Joint ALMA Observatory is operated by ESO, AUI/NRAO and NAOJ. The National Radio Astronomy Observatory is a facility of the National Science Foundation operated under cooperative agreement by Associated Universities, Inc. We are grateful to the CFHT and ALMA scheduling, data processing and archive teams. We also wish to acknowledge that the summit of Maunakea is a significant cultural and historic site for the indigenous Hawaiian community, while the high-altitude plateau Chajnantor on which the ALMA telescope sits is sacred to indigenous Likanantai people. We are most grateful to have the opportunity of observing there. This paper also makes use of observations made with the NASA/ESA *Hubble Space Telescope* and the NASA/IPAC Extragalactic Database (NED).

AL, HB, DH, and LD acknowledge funding from the NSERC Discovery Grant and the Canada Research Chairs (CRC) programme. HB is grateful for support from the Natural Sciences and Engineering Research Council of Canada (NSERC) Alexander Graham Bell Canada Graduate Scholarship. LC acknowledges support by the ANID/FONDECYT Regular Project 1210992. MC and JMDK gratefully acknowledge funding from the German Research Foundation (DFG) through an Emmy Noether Grant (grant number KR4801/1-1), as well as from the European Research Council (ERC) under the European Union's Horizon 2020 research and innovation programme via the ERC Starting Grant MUSTANG (grant agreement number 714907). TAD and IR acknowledge support from the UK Science and Technology Facilities Council through grants ST/S00033X/1 and

ST/W000830/1. JG gratefully acknowledges financial support from the Swiss National Science Foundation (grant no CRSII5\_193826). TGW acknowledges funding from the European Research Council (ERC) under the European Union's Horizon 2020 research and innovation programme (grant agreement No. 694343).

## DATA AVAILABILITY

The raw data underlying this article are publicly available on NRAO and CFHT archive. All analysed data are available in the article and upon request.

## REFERENCES

- Athanassoula E., Bureau M., 1999, *ApJ*, 522, 699  
 Baldwin J. A., Phillips M. M., Terlevich R., 1981, *PASP*, 93, 5  
 Barrera-Ballesteros J. K., Sanchez S., Heckman T., Bolatto A., Wong T., 2021, Extragalactic Spectroscopic Surveys: Past, Present and Future of Galaxy Evolution (GALSPEC2021). Zenodo. Available at: <https://doi.org/10.5281/zenodo.4721500>  
 Bertoldi F., McKee C. F., 1992, *ApJ*, 395, 140  
 Bigiel F., Leroy A., Walter F., Brinks E., De Blok W., Madore B., Thornley M. D., 2008, *AJ*, 136, 2846  
 Bolatto A. D., Wolfire M., Leroy A. K., 2013, *ARA&A*, 51, 207  
 Bouché N. et al., 2010, *ApJ*, 718, 1001  
 Brinchmann J., Charlot S., White S. D., Tremonti C., Kauffmann G., Heckman T., Brinkmann J., 2004, *MNRAS*, 351, 1151  
 Bureau M., Freeman K., 1999, *AJ*, 118, 126  
 Buta R., Combes F., 1996, *Fund. Cosmic Phys.*, 17, 95  
 Buta R., Purcell G. B., 1998, *AJ*, 115, 484  
 Chen J. et al., 2019, *MNRAS*, 489, 855  
 Chevance M. et al., 2020, *MNRAS*, 493, 2872  
 Chevance M. et al., 2022, *MNRAS*, 509, 272  
 Comerón S. et al., 2014, *A&A*, 562, A121  
 Davé R., Finlator K., Oppenheimer B. D., 2012, *MNRAS*, 421, 98  
 Davis T. A. et al., 2013, *MNRAS*, 429, 534  
 Davis T. A. et al., 2014, *MNRAS*, 444, 3427  
 Decarli R. et al., 2016, *ApJ*, 833, 69  
 Deconto-Machado A. et al., 2022, *A&A*, 659, A131  
 de Vaucouleurs G., de Vaucouleurs A., Corwin H. G. J., Buta R. J., Paturel G., Fouque P., 1991, *Third Reference Catalogue of Bright Galaxies*. Springer, Berlin  
 Domínguez-Fernández A. et al., 2020, *A&A*, 643, A127  
 Dong X., De Robertis M. M., 2006, *AJ*, 131, 1236  
 Drissen L. et al., 2019, *MNRAS*, 485, 3930  
 Feldmann R., Mayer L., 2015, *MNRAS*, 446, 1939  
 Fitzpatrick E. L., 1986, *AJ*, 92, 1068  
 Foreman-Mackey D., Hogg D. W., Lang D., Goodman J., 2013, *PASP*, 125, 306  
 Fujimoto Y., Chevance M., Haydon D. T., Krumholz M. R., Kruijssen J. M. D., 2019, *MNRAS*, 487, 1717  
 Gao Y., Egusa F., Liu G., Kohno K., Bao M., Morokuma-Matsui K., Kong X., Chen X., 2021, *ApJ*, 913, 139  
 Gensior J., Kruijssen J. D., 2021, *MNRAS*, 500, 2000  
 Gensior J., Kruijssen J. D., Keller B. W., 2020, *MNRAS*, 495, 199  
 Genzel R. et al., 2010, *MNRAS*, 407, 2091  
 Ghosh H., Mathur S., Fiore F., Ferrarese L., 2008, *ApJ*, 687, 216  
 Haydon D. T., Kruijssen J. D., Chevance M., Hygate A. P., Krumholz M. R., Schruha A., Longmore S. N., 2020, *MNRAS*, 498, 235  
 Héraudeau P., Simien F., Maubon G., Prugniel P., 1999, *A&AS*, 136, 509  
 Ho L. C., Filippenko A. V., Sargent W. L., 1997, *ApJS*, 112, 315  
 Hughes A. et al., 2013, *ApJ*, 779, 44  
 Hygate A. P., Kruijssen J. D., Chevance M., Schruha A., Haydon D. T., Longmore S. N., 2019, *MNRAS*, 488, 2800  
 Jarrett T., Chester T., Cutri R., Schneider S., Huchra J., 2003, *AJ*, 125, 525

- Jeffreson S. M. R., Krumholz M. R., Fujimoto Y., Armillotta L., Keller B. W., Chevance M., Kruijssen J. M. D., 2021, *MNRAS*, 505, 3470
- Kennicutt R. C., Jr, 1998, *ApJ*, 498, 541
- Kennicutt R. C., Jr, De Los Reyes M. A., 2021, *ApJ*, 908, 61
- Kennicutt R. C., Jr, Evans N. J., 2012, *ARA&A*, 50, 531
- Kewley L. J., Groves B., Kauffmann G., Heckman T., 2006, *MNRAS*, 372, 961
- Kim J. et al., 2021, *MNRAS*, 504, 487
- Kormendy J., Ho L. C., 2013, *ARA&A*, 51, 511
- Kruijssen J. M. D., Longmore S. N., 2014, *MNRAS*, 439, 3239
- Kruijssen J. D., Longmore S. N., Elmegreen B. G., Murray N., Bally J., Testi L., Kennicutt R. C., Jr, 2014, *MNRAS*, 440, 3370
- Kruijssen J. M. D., Schrubba A., Hygate A. P. S., Hu C.-Y., Haydon D. T., Longmore S. N., 2018, *MNRAS*, 479, 1866
- Kruijssen J. M. D. et al., 2019a, *MNRAS*, 484, 5734
- Kruijssen J. M. D. et al., 2019b, *Nature*, 569, 519
- Lamperti I. et al., 2020, *ApJ*, 889, 103
- Lang P. et al., 2014, *ApJ*, 788, 11
- Law D. R. et al., 2021, *ApJ*, 915, 35
- Lee-Waddell K., Spekkens K., Haynes M. P., Stierwalt S., Chengalur J., Chandra P., Giovanelli R., 2012, *MNRAS*, 427, 2314
- Leroy A. K. et al., 2019, *ApJS*, 244, 24
- Levy R. C. et al., 2018, *ApJ*, 860, 92
- Lindegren L. et al., 2018, *A&A*, 616, A2
- Liu L., Bureau M., Blitz L., Davis T. A., Onishi K., Smith M., North E., Iguchi S., 2021, *MNRAS*, 505, 4048
- Longmore S. et al., 2013, *MNRAS*, 429, 987
- McMullin J. P., Waters B., Schiebel D., Young W., Golap K., 2007, in Shaw R. A., Hill F., Bell D. J., eds, ASP Conf. Ser. Vol. 376, *Astronomical Data Analysis Software and Systems XVI*. Astron. Soc. Pac., San Francisco, p. 127
- Martig M., Bournaud F., Teyssier R., Dekel A., 2009, *ApJ*, 707, 250
- Martig M. et al., 2013, *MNRAS*, 432, 1914
- Martin T., Drissen L., Joncas G., 2015, in Taylor A. R., Rosolowsky E., eds, ASP Conf. Ser. Vol. 495, *Astronomical Data Analysis Software and Systems XXIV*. Astron. Soc. Pac., San Francisco, p. 327
- Martin T. B., Prunet S., Drissen L., 2016, *MNRAS*, 463, 4223
- Martin T., Drissen L., Prunet S., 2021, *MNRAS*, 505, 5514
- Mathur S., Ghosh H., Ferrarese L., Fiore F., 2008, *AIP Conf. Proc.*, 1053, 43
- Moustakas J. et al., 2013, *ApJ*, 767, 50
- Nagar N. M., Falcke H., Wilson A. S., 2005, *A&A*, 435, 521
- Nelson E. J. et al., 2016, *ApJ*, 817, L9
- Noeske K. et al., 2007, *ApJ*, 660, L43
- Onishi K., Iguchi S., Davis T. A., Bureau M., Cappellari M., Sarzi M., Blitz L., 2017, *MNRAS*, 468, 4663
- Osterbrock D. E., Ferland G. J., 2006, *Astrophysics of Gaseous Nebulae and Active Galactic Nuclei*, 2nd edn. University Science Books, Sausalito, CA
- Pan H.-A. et al., 2022, *ApJ*, 927, 9
- Peng C. Y., Ho L. C., Impey C. D., Rix H.-W., 2002, *AJ*, 124, 266
- Pontzen A., Tremmel M., Roth N., Peiris H. V., Saintonge A., Volonteri M., Quinn T., Governato F., 2017, *MNRAS*, 465, 547
- Querejeta M. et al., 2019, *A&A*, 625, A19
- Renaud F. et al., 2015, *MNRAS*, 454, 3299
- Rodighiero G. et al., 2011, *ApJ*, 739, L40
- Rosolowsky E., 2007, *ApJ*, 654, 240
- Rosolowsky E., Leroy A., 2006, *PASP*, 118, 590
- Rosolowsky E., Engargiola G., Plambeck R., Blitz L., 2003, *ApJ*, 599, 258
- Rousseau-Nepton L., Robert C., Martin R., Drissen L., Martin T., 2018, *MNRAS*, 477, 4152
- Ruffa I., Prandoni I., Davis T. A., Laing R. A., Paladino R., Casasola V., Parma P., Bureau M., 2022, *MNRAS*, 510, 4485
- Saintonge A. et al., 2011, *MNRAS*, 415, 61
- Sato K., Miyamoto Y., Kuno N., Salak D., Wagner A. Y., Seta M., Nakai N., 2021, *PASJ*, 73, 1019
- Schinnerer E. et al., 2019, *The Messenger*, 177, 36
- Schruba A., Leroy A. K., Walter F., Sandstrom K., Rosolowsky E., 2010, *ApJ*, 722, 1699
- Sil'chenko O., Afanasiev V., 2006, *Astron. Lett.*, 32, 534
- Speagle J. S., Steinhardt C. L., Capak P. L., Silverman J. D., 2014, *ApJS*, 214, 15
- Steer I. et al., 2017, *AJ*, 153, 37
- Strong A. et al., 1988, *A&A*, 207, 1
- Sun J. et al., 2018, *ApJ*, 860, 172
- Sun J. et al., 2020, *ApJ*, 901, L8
- Teodoro E. D., Fraternali F., 2015, *MNRAS*, 451, 3021
- Utomo D., Blitz L., Davis T., Rosolowsky E., Bureau M., Cappellari M., Sarzi M., 2015, *ApJ*, 803, 16
- Venturi G. et al., 2021, *A&A*, 648, A17
- Ward J. L., Chevance M., Kruijssen J. M. D., Hygate A. P. S., Schrubba A., Longmore S. N., 2020, *MNRAS*, 497, 2286
- Zabel N. et al., 2020, *MNRAS*, 496, 2155
- Zaragoza-Cardiel J. et al., 2015, *MNRAS*, 451, 1307

## APPENDIX A: IONIZATION MECHANISM CLASSIFICATION IN A 3D LINE RATIO SPACE

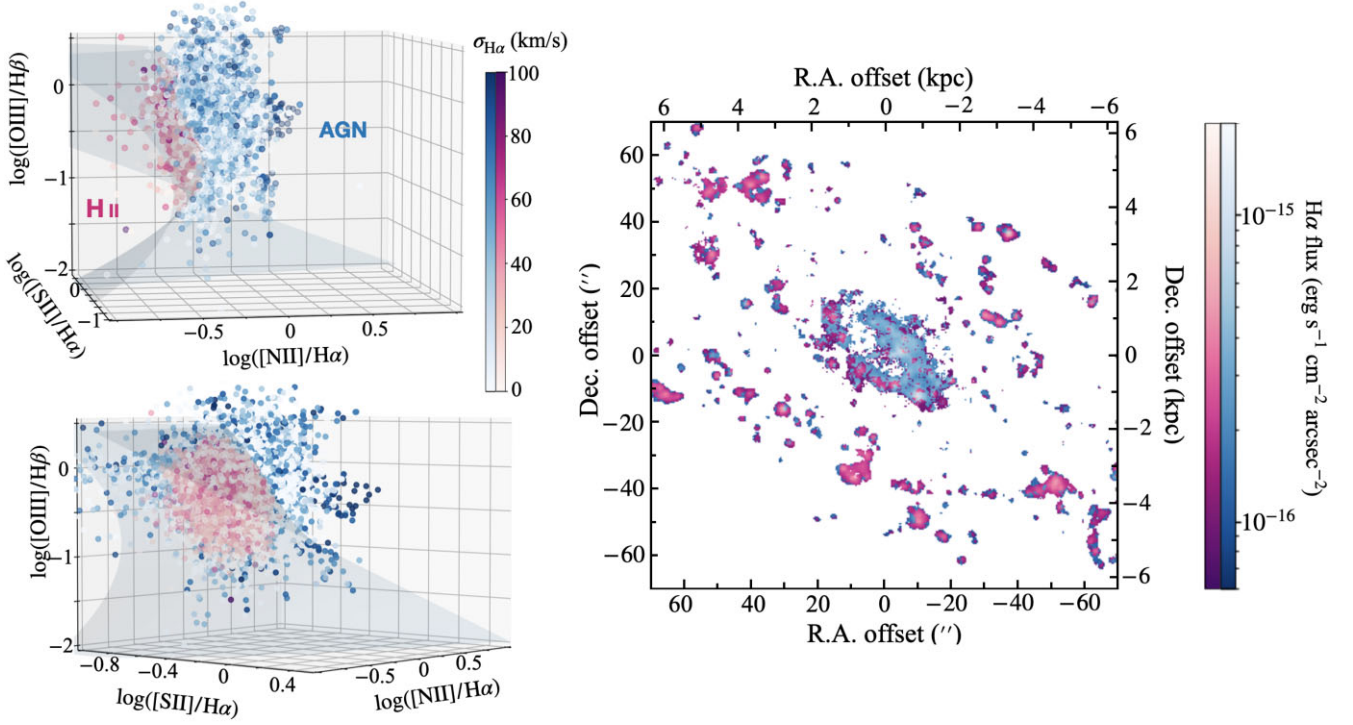


**Figure A1.** Ionization-mechanism classification over the whole disc of NGC 3169 in a 3D line ratio space. Left-hand panel: 3D plot of the line ratios  $[O\ III]/H\beta$ ,  $[N\ II]/H\alpha$  and  $[S\ II]/H\alpha$ . AGN/LINER-ionized (blue) and  $H\ II$  (pink) regions are separated using a plane defined by equation (11) and table 2 in Law et al. (2021). The colour gradient shows the broadening of the  $H\alpha$  line, indicative of gas temperature and associated ionization mechanism. The top and bottom plots illustrate different directions of viewing the same parameter space. Right-hand panel: the  $H\alpha$  flux map colour-coded according to the region separation shown in the left-panel panels, as a comparison to the right-hand panels of Fig. 4.

## APPENDIX B: $H\ II$ CATALOGUE

**Table B1.** Catalogue of all  $H\ II$  region parameters discussed in Section 4.4.

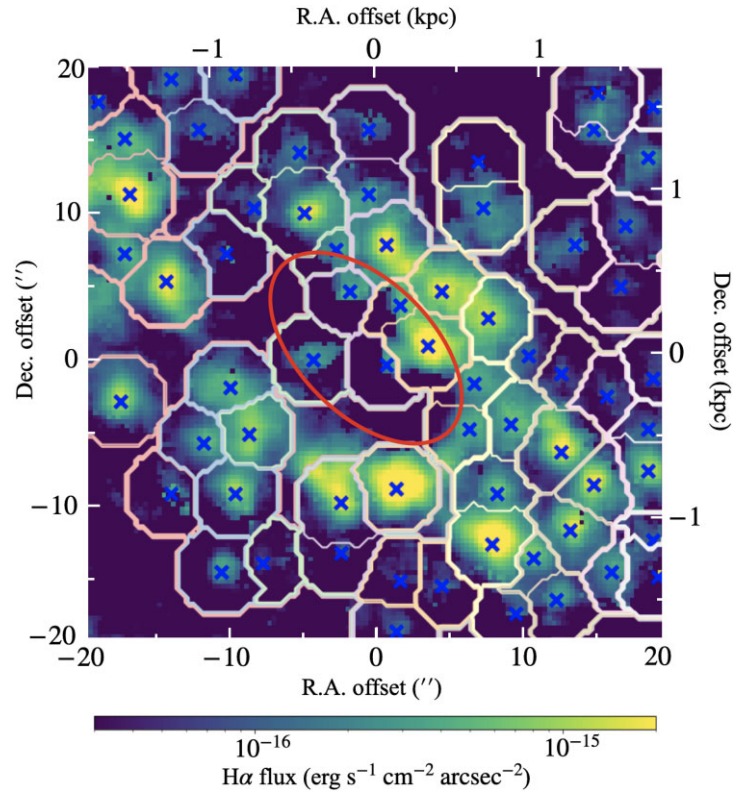
| ID | RA<br>( $^{\circ}$ ) | Dec.<br>( $^{\circ}$ ) | $R_{H\ II}$<br>(pc) | $R_G$<br>(kpc) | $\log(L_{H\ II}/\text{erg s}^{-1})$<br>– | $M_{H\ II}$<br>( $\times 10^3 M_{\odot}$ ) | $V_{\text{avg}, H\ II}$<br>( $\text{km s}^{-1}$ ) | $\sigma_{H\ II}$<br>( $\text{km s}^{-1}$ ) | $\log(\alpha_{\text{vir}, H\ II})$<br>– | $\tau_{\text{dep}, H\ II}$<br>(Gyr) |
|----|----------------------|------------------------|---------------------|----------------|--|--|---|--|---|-------------------------------------|
| 0  | 153.565              | 3.463                  | <100                | 2.61           | 36.8                                     | 46   | 1360  | N/A  | N/A                                     | N/A                                 |
| 1  | 153.569              | 3.463                  | <100                | 2.71           | 36.8                                     | 46   | 1548  | 68   | 4.11                                    | N/A                                 |
| 2  | 153.568              | 3.463                  | <100                | 2.42           | 36.9                                     | 50   | 1492  | 30   | 3.36                                    | N/A                                 |
| 3  | 153.562              | 3.464                  | <100                | 3.26           | 37.0                                     | 55   | 1303  | N/A  | N/A                                     | 0.39                                |
| 4  | 153.569              | 3.464                  | 145                 | 2.53           | 37.7                                     | 197  | 1497  | 32   | 2.94                                    | N/A                                 |
| 5  | 153.568              | 3.464                  | 237                 | 2.07           | 37.6                                     | 349  | 1495  | 39   | 3.08                                    | 0.69                                |
| 6  | 153.567              | 3.464                  | 193                 | 1.79           | 38.6                                     | 845  | 1470  | 28   | 2.33                                    | 0.19                                |
| 7  | 153.568              | 3.465                  | 146                 | 2.08           | 38.3                                     | 373  | 1498  | 21   | 2.29                                    | 0.45                                |
| 8  | 153.564              | 3.465                  | 187                 | 1.73           | 38.2                                     | 489  | 1330  | 21   | 2.31                                    | 0.16                                |
| 9  | 153.562              | 3.465                  | 138                 | 2.42           | 38.1                                     | 272  | 1278  | 21   | 2.42                                    | 0.14                                |
| 10 | 153.565              | 3.465                  | 249                 | 1.34           | 38.3                                     | 861  | 1397  | 33   | 2.57                                    | 0.12                                |
| 11 | 153.567              | 3.465                  | 154                 | 1.43           | 37.7                                     | 206  | 1493  | 33   | 2.96                                    | 1.85                                |
| 12 | 153.569              | 3.465                  | 138                 | 2.07           | 38.0                                     | 270  | 1491  | 37   | 2.91                                    | 0.20                                |
| 13 | 153.563              | 3.466                  | 204                 | 1.59           | 38.0                                     | 452  | 1303  | 19   | 2.30                                    | 0.14                                |
| 14 | 153.565              | 3.466                  | 205                 | 1.15           | 38.3                                     | 658  | 1393  | 28   | 2.46                                    | 0.15                                |
| 15 | 153.566              | 3.466                  | 227                 | 1.13           | 37.6                                     | 339  | 1474  | 52   | 3.32                                    | 1.67                                |
| 16 | 153.570              | 3.466                  | 147                 | 2.56           | 38.2                                     | 351  | 1444  | 27   | 2.55                                    | N/A                                 |
| 17 | 153.564              | 3.466                  | 210                 | 1.30           | 37.9                                     | 421  | 1350  | 19   | 2.31                                    | 0.26                                |
| 18 | 153.568              | 3.466                  | 104                 | 1.78           | 38.8                                     | 406  | 1466  | 33   | 2.52                                    | 0.28                                |
| 19 | 153.561              | 3.466                  | 167                 | 2.26           | 37.9                                     | 305  | 1259  | 24   | 2.57                                    | 0.20                                |
| 20 | 153.562              | 3.467                  | 309                 | 1.77           | 37.9                                     | 722  | 1251  | 24   | 2.45                                    | 0.15                                |
| 21 | 153.560              | 3.466                  | <100                | 2.62           | 36.8                                     | 46   | 1230  | N/A  | N/A                                     | 0.56                                |
| 22 | 153.567              | 3.467                  | 226                 | 1.42           | 37.5                                     | 298  | 1423  | 29   | 2.88                                    | 0.40                                |



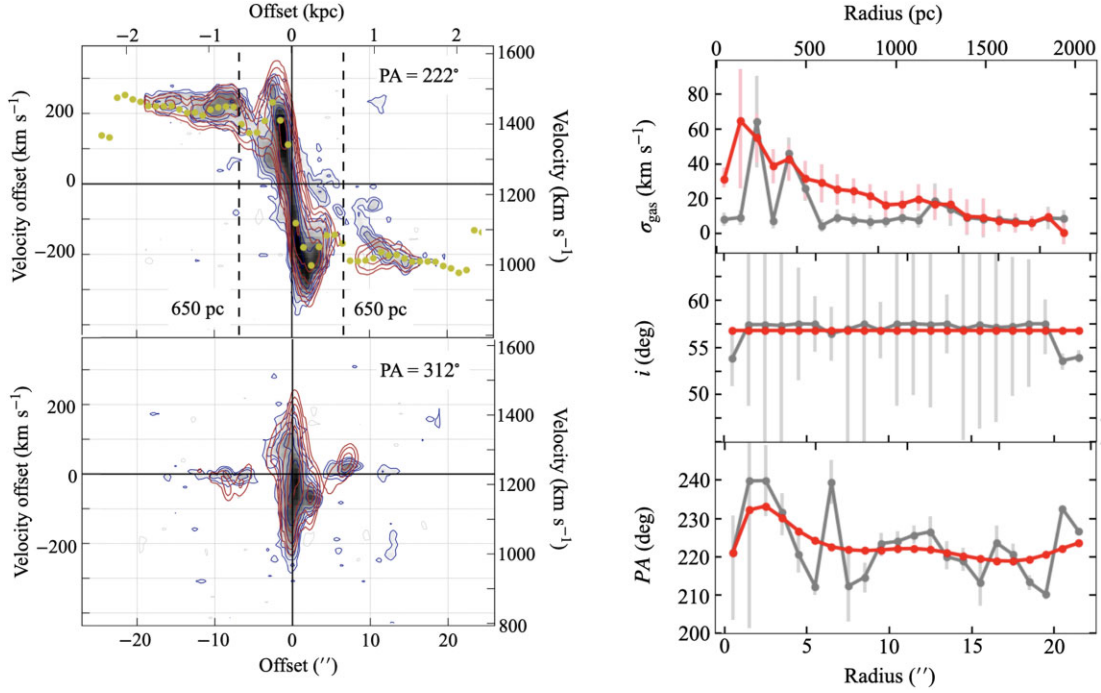
**Table B1** – *continued*

| ID | RA             | Dec.           | $R_{\text{H II}}$ | $R_{\text{G}}$ | $\log(L_{\text{H II}}/\text{erg s}^{-1})$ | $M_{\text{H II}}$           | $V_{\text{avg,H II}}$  | $\sigma_{\text{H II}}$ | $\log(\alpha_{\text{vir,H II}})$ | $\tau_{\text{dep,H II}}$ |
|----|----------------|----------------|-------------------|----------------|---|-----------------------------|------------------------|------------------------|----------------------------------|--------------------------|
| –  | ( $^{\circ}$ ) | ( $^{\circ}$ ) | (pc)              | (kpc)          | –   | ( $\times 10^3 M_{\odot}$ ) | ( $\text{km s}^{-1}$ ) | ( $\text{km s}^{-1}$ ) | –                                | (Gyr)                    |
| 23 | 153.567        | 3.467          | 179               | 1.00           | 37.7                                      | 273                         | 1410                   | 38                     | 3.05                             | 1.12                     |
| 24 | 153.563        | 3.467          | 272               | 1.25           | 37.5                                      | 389                         | 1284                   | 22                     | 2.61                             | 0.70                     |
| 25 | 153.568        | 3.467          | 186               | 1.63           | 37.7                                      | 289                         | 1392                   | 24                     | 2.65                             | 0.53                     |
| 26 | 153.560        | 3.467          | 178               | 2.81           | 38.1                                      | 404                         | 1226                   | 16                     | 2.10                             | 0.21                     |
| 27 | 153.561        | 3.467          | <100              | 1.83           | 37.2                                      | 74                          | 1208                   | 23                     | 2.96                             | 0.32                     |
| 28 | 153.567        | 3.467          | <100              | 1.45           | 37.2                                      | 70                          | 1379                   | 37                     | 3.39                             | 1.29                     |
| 29 | 153.562        | 3.467          | 335               | 1.53           | 37.4                                      | 491                         | 1199                   | 22                     | 2.57                             | 0.30                     |
| 30 | 153.567        | 3.467          | <100              | 1.08           | 36.9                                      | 51                          | 1389                   | 17                     | 2.88                             | 1.06                     |
| 31 | 153.560        | 3.468          | <100              | 2.18           | 36.8                                      | 46                          | 1175                   | N/A                    | N/A                              | 1.58                     |
| 32 | 153.563        | 3.468          | <100              | 0.67           | 36.8                                      | 47                          | 1190                   | 90                     | 4.34                             | 0.79                     |
| 33 | 153.564        | 3.468          | <100              | 0.11           | 36.9                                      | 50                          | 1356                   | 108                    | 4.47                             | 11.77                    |
| 34 | 153.567        | 3.468          | <100              | 1.52           | 37.1                                      | 62                          | 1348                   | 39                     | 3.49                             | 0.94                     |
| 35 | 153.566        | 3.468          | 181               | 0.81           | 38.7                                      | 808                         | 1322                   | 45                     | 2.73                             | 0.48                     |
| 36 | 153.564        | 3.468          | <100              | 0.25           | 36.8                                      | 46                          | 1158                   | N/A                    | N/A                              | 5.40                     |
| 37 | 153.567        | 3.469          | 200               | 1.56           | 38.4                                      | 740                         | 1308                   | 32                     | 2.49                             | 0.15                     |
| 38 | 153.561        | 3.469          | <100              | 1.53           | 37.3                                      | 81                          | 1130                   | 26                     | 3.02                             | 1.23                     |
| 39 | 153.561        | 3.469          | 227               | 1.86           | 38.2                                      | 657                         | <1108                  | 27                     | 2.46                             | 0.15                     |
| 40 | 153.566        | 3.469          | 226               | 1.52           | 38.4                                      | 852                         | 1278                   | 29                     | 2.40                             | 0.14                     |
| 41 | 153.565        | 3.470          | 213               | 1.24           | 37.7                                      | 360                         | 1238                   | 33                     | 2.87                             | 0.15                     |
| 42 | 153.560        | 3.470          | 337               | 2.28           | 37.5                                      | 557                         | 1123                   | 39                     | 3.02                             | 0.09                     |
| 43 | 153.565        | 3.470          | 281               | 1.37           | 37.5                                      | 440                         | 1206                   | 38                     | 3.03                             | 0.26                     |
| 44 | 153.560        | 3.470          | 321               | 2.33           | 37.6                                      | 588                         | 1079                   | 29                     | 2.73                             | 0.01                     |
| 45 | 153.569        | 3.470          | <100              | 3.55           | 36.8                                      | 46                          | 1298                   | N/A                    | N/A                              | N/A                      |
| 46 | 153.567        | 3.470          | 182               | 2.47           | 37.6                                      | 244                         | 1259                   | 28                     | 2.85                             | 0.24                     |
| 47 | 153.563        | 3.471          | 342               | 1.42           | 37.4                                      | 470                         | 1149                   | 24                     | 2.69                             | 0.68                     |
| 48 | 153.564        | 3.471          | <100              | 1.79           | 36.9                                      | 49                          | 1195                   | 33                     | 3.46                             | 0.56                     |
| 49 | 153.560        | 3.471          | 198               | 2.29           | 38.6                                      | 829                         | 1050                   | 30                     | 2.40                             | 0.15                     |
| 50 | 153.566        | 3.471          | <100              | 2.49           | 37.3                                      | 84                          | 1251                   | N/A                    | N/A                              | 0.02                     |
| 51 | 153.559        | 3.472          | <100              | 2.66           | 37.8                                      | 146                         | 1042                   | 27                     | 2.81                             | N/A                      |
| 52 | 153.570        | 3.472          | <100              | 4.36           | 37.0                                      | 58                          | 1303                   | N/A                    | N/A                              | N/A                      |
| 53 | 153.563        | 3.472          | <100              | 2.06           | 36.8                                      | 47                          | 1145                   | 32                     | 3.45                             | 0.52                     |
| 54 | 153.560        | 3.472          | <100              | 2.38           | 37.4                                      | 89                          | 1046                   | 14                     | 2.43                             | N/A                      |
| 55 | 153.570        | 3.472          | <100              | 4.80           | 36.8                                      | 46                          | 1290                   | N/A                    | N/A                              | N/A                      |
| 56 | 153.561        | 3.473          | <100              | 2.77           | 37.0                                      | 56                          | 1088                   | 23                     | 3.09                             | N/A                      |
| 57 | 153.562        | 3.473          | <100              | 2.74           | 36.8                                      | 46                          | 1112                   | 12                     | 2.58                             | N/A                      |

*Notes.* Column 2 and 3: RA and Dec. are sky coordinates. Column 4: galactocentric radius ( $R_{\text{G}}$ ). Column 5:  $\text{H}\alpha$  luminosity of the  $\text{H II}$  regions ( $\log(L_{\text{H II}})$ ). Column 6: ionized gas mass ( $M_{\text{H II}}$ ). Column 7: mean line of sight velocity ( $V_{\text{avg,H II}}$ ). Column 8: velocity dispersion ( $\sigma_{\text{H II}}$ ). Column 9: virial parameter ( $\log(\alpha_{\text{vir,H II}})$ ). Column 10: depletion time  $\tau_{\text{dep,H II}}$ . More parameters and/or parameters for the whole field of view of SITELLE can be provided upon request.



**Figure B1.** Boundaries (white lines) and centres (blue crosses) of the H II regions identified in Section 4.4, overlaid on the H $\alpha$  flux map. The red ellipse separates the inner disc and outer star-forming ring discussed in Sections 4–5.

**APPENDIX C: THE BEST-FITTING  
MOLECULAR GAS KINEMATICS MODEL**


**Figure C1.** Left-hand panel: PV diagrams of the CO emission along the major axis (top panel; at  $PA = 224^\circ$ ) and minor axis (bottom panel; at  $314^\circ$ ). Shaded blue contours show the observed velocities, while red contours show the best-fitting models from 3DBAROLO. Overlaid yellow circles indicate the best-fitting rotation velocities. Right-hand panel: radial profiles of the velocity dispersion [ $\sigma_{\text{gas}}$  (top panel), inclination ( $i$ ; middle right-hand panel) and position angle ( $PA$ ; bottom right-hand panel), from the best-fitting 3DBAROLO model assuming a fixed systemic (heliocentric) velocity of  $1230 \text{ km s}^{-1}$ . Grey data points are from a fit with all these parameters free, while red data points are from a fit with  $i$  and  $PA$  kept fixed.



APPENDIX D: LIFECYCLE OF MOLECULAR CLOUDS

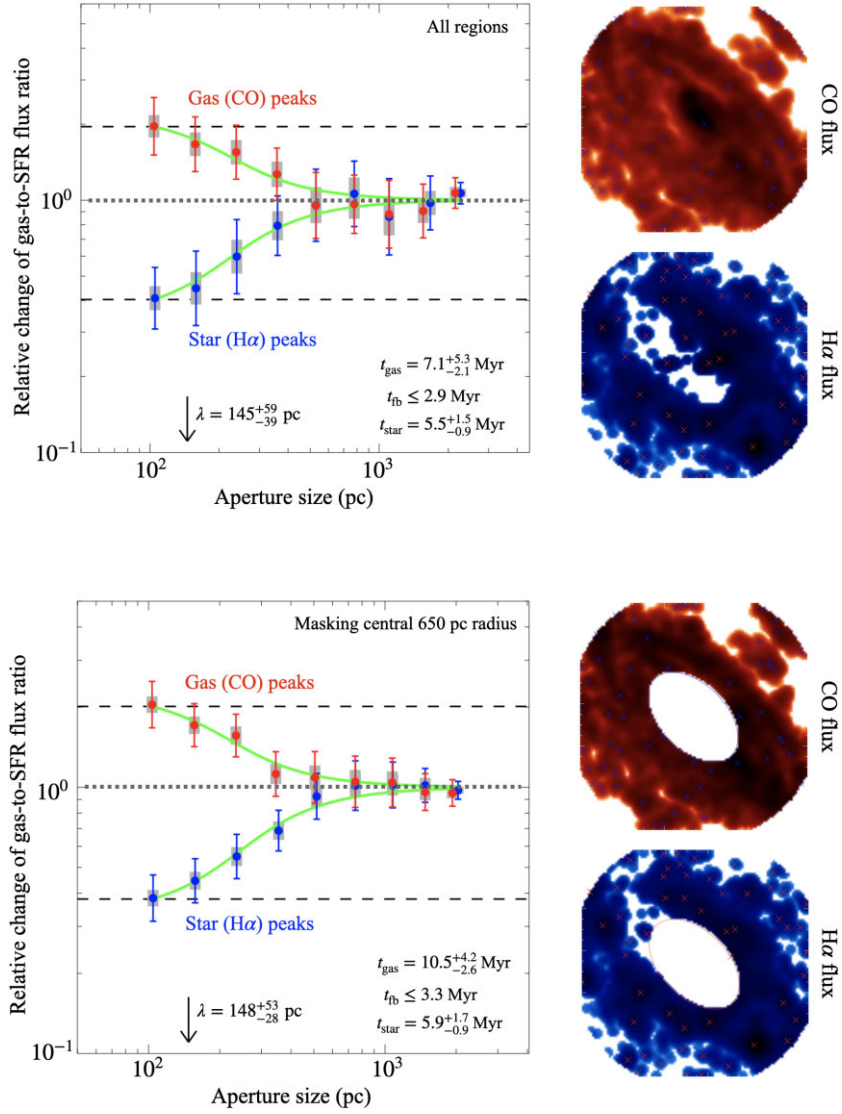


Figure D1. Same as Fig. 10 but for Cases A (top panel) and B (bottom panel).

This paper has been typeset from a  $\text{\TeX}/\text{\LaTeX}$  file prepared by the author.